Chapter 3 Shielding of Proton and Ion Accelerators

In this chapter the major considerations pertinent to the shielding of proton and ion accelerators are addressed. Particular emphasis is placed on the shielding of neutrons in view of their general dominance of the radiation fields. The shielding of muons at such accelerators is also described. A short review of the various Monte-Carlo programs commonly used in shielding calculations at proton and ion accelerators is presented. The properties of various shielding materials commonly used at accelerators are reviewed. The chapter concludes with a discussion of various features of neutron energy spectra found at proton accelerators.

I. Hadron (Neutron) Shielding for Low Energy Incident Protons

For this discussion, the "low energy" region extends up to approximately E_0 = 100 MeV. The basic treatment is similar to that generally followed by Patterson and Thomas (Pa73).

$E_0 \leq$ 15 MeV:

This region is especially complex because it is the region of significant nuclear structure effects. There are many resonances associated with compound nucleus that can be excited and there also many nuclear reaction channels leading to a large number of nuclear excited states up to 20 MeV in excitation energy which have a wide variety of nuclear structure quantum numbers and very narrow widths in energy.

The method most commonly used to calculate shielding thicknesses is that of **removal cross section theory**.

According to Clark (Cl71) there are three principles involved here:

A. "The shield must be sufficiently thick and the neutrons so distributed in energy that only a narrow band of the most penetrating source neutrons give any appreciable ultimate contribution to the dose outside the shield."

B. "There must be sufficient hydrogen in the shield, intimately mixed or in the final shield region, to asssure a very short characteristic transport length from about one MeV to absorption at or near thermal energy."

C. "The source energy distribution and shield material (nonhydrogeneous) properties must be such as to assure a short transport distance for slowing down from the most penetrating energies to 1 MeV."

It has been found that the transmission of dose equivalent, H, as a function of shield thickness, t, is approximately given for these neutrons by

$$H(t) = \Phi_0 PG \exp(-\Sigma_r t), \tag{3.1}$$

where Φ_0 is the fluence before the shielding (calculated from neutron yield information), P is the dose equivalent per fluence conversion factor (obtained by performing any needed integration over the energy spectrum), G is a "geometry factor", t (cm) is the thickness of the shield. For parallel beams, $G = 1$ while for an isotropic point source, $G = 1/r^2$. Σ_r is the **macroscopic removal cross section**:

$$\Sigma_r = \frac{0.602\sigma_r\rho}{A}, \tag{3.2}$$

where σ_r is the microscopic removal cross section in barns, ρ is the density (g/cm^3) and A is the mass number. For mixtures of n materials,

$$\Sigma_r = \sum_{i=1}^{n}\left(\frac{\Sigma_{ri}}{\rho}\right)_i \rho_i \tag{3.3}$$

where the quantity in parentheses is the **removal cross section per unit mass** of the i^{th} constituent and ρ_i is the **partial density** of the i^{th} material. In this formulation the overall density is equal to the sum of the partial densities.

For $A > 8$,

$$\sigma_r \approx 0.21\, A^{-0.58} \quad \text{(barns)} \tag{3.4}$$

for neutrons of approximately 8 MeV. Figure 3.1 taken from (Pa73) shows the values of σ_r as a function of mass number at this energy. Table 3.1 gives representative values for σ_r for some energies where this approach is applicable. The use of removal cross sections describe attenuation data rather effectively despite the fact that as more shielding is penetrated, neutrons of lower energy tend to dominate the spectrum over those in the few MeV region.

Table 3.1 Removal cross-section data, σ_r (barns) for low energy neutrons. The typical accuracy is quoted to be ± 5 %. [Adapted from (Pa73).]

Element	1 MeV	Fission Spectrum	2.9 MeV	4 MeV	6.7 MeV	14.9 MeV
Carbon		0.9	1.58	1.05	0.83	0.50
Aluminum		1.31				
Iron	1.1	1.96	1.94	1.98	2.26	1.60
Copper		2.04				
Lead		3.28	2.70	3.44	3.77	2.95

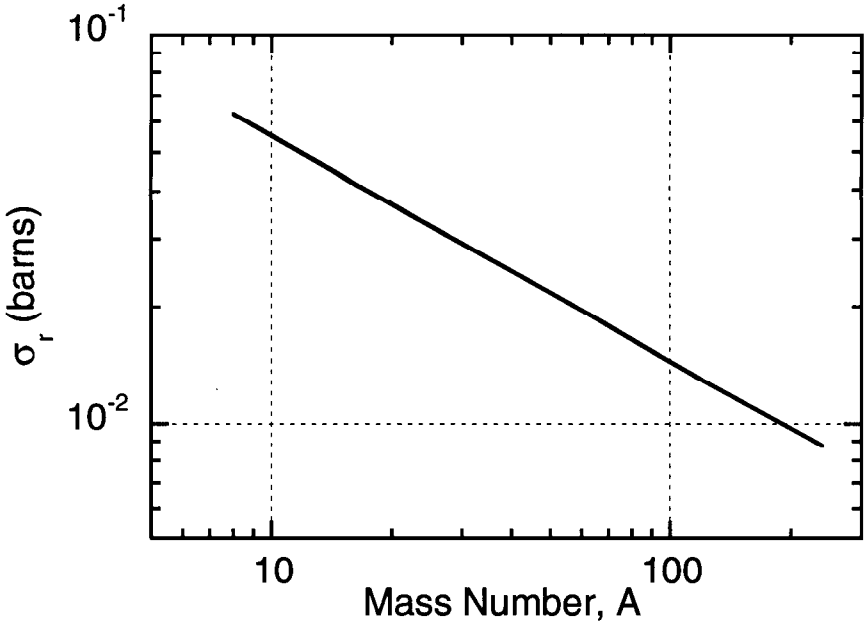

Fig. 3.1 Removal cross sections per unit atomic mass for fission neutrons as a function of mass number at a neutron energy of 8 MeV. Over the range $8 \leq A \leq 240$, the values are well fit by Eq. (3.4). [Adapted from (Pa73)].

II. Limiting Attenuation at High Energy

The most important feature of neutron shielding at accelerators is the fact of limiting attenuation at high energy. As the energy increases, the neutron inelastic cross sections also increase rapidly until about 25 MeV where they level off and then fall rapidly with energy in the region $25 < E_n < 100$ MeV to a value which becomes independent of energy. This observation was first made by Lindenbaum (Li61). The result is that high energy neutron beams attenuate approximately exponentially with an attenuation length, λ_{atten}, which is rather insensitive to energy. Thus, in units of length,

$$\lambda_{atten} = \frac{1}{N\sigma_{in}} \tag{3.5}$$

where σ_{in} is the inelastic cross section, roughly equivalent to the so-called "absorption cross section" and N is the number of absorber nuclei per unit volume. This cross section specifically does not include elastic scattering and so is always smaller than the total cross section. N is the number of atoms of the absorbing material per unit volume determined as in Chapter 1 in association with Eq. (1.6). In a "simple-minded" approach, this cross section can be taken to be approximately geometric and the nucleon radius is taken to be 1.2×10^{-13} cm. It then follows that in the high energy limit, one can multiply by the density to get:

$$\rho\lambda_{atten} = 38A^{1/3} \quad (\text{g/cm}^2). \tag{3.6}$$

Fig. 3.2 (Li61) illustrates the neutron inelastic cross sections for several materials up to a kinetic energy of 1.4 GeV. These results are well-represented by

$$\sigma_{in} = 43A^{0.69} \quad (\text{mb}), \tag{3.7}$$

which was initially verified by cosmic ray results.

The **interaction length**, λ_{inel} (g/cm^2), is thus given by:

$$\lambda_{inel} = \frac{\rho}{N\sigma_{in}} = 38.5A^{0.31} \ (\text{g/cm}^2) \tag{3.8}$$

The geometric approximation is thus reasonably accurate. Tabular values of the high energy interaction lengths are available for many different materials and representative examples are found in Table 1.2. Figure 3.3 shows the results for absorption cross sections based upon these values.

Schopper et al. (Sc90) has provided extensive tabulations of the value of σ_{in} (mb) for a variety of particles, energies, and materials in the high energy region as functions of particle momenta up to 10 TeV/c. The saturation of attenuation length for concrete as a function of particle energy is especially important. Figure 3.4 gives the results for both neutrons and protons. An important feature of these results is the equivalence of the attenuation lengths for protons and neutrons at high energies.

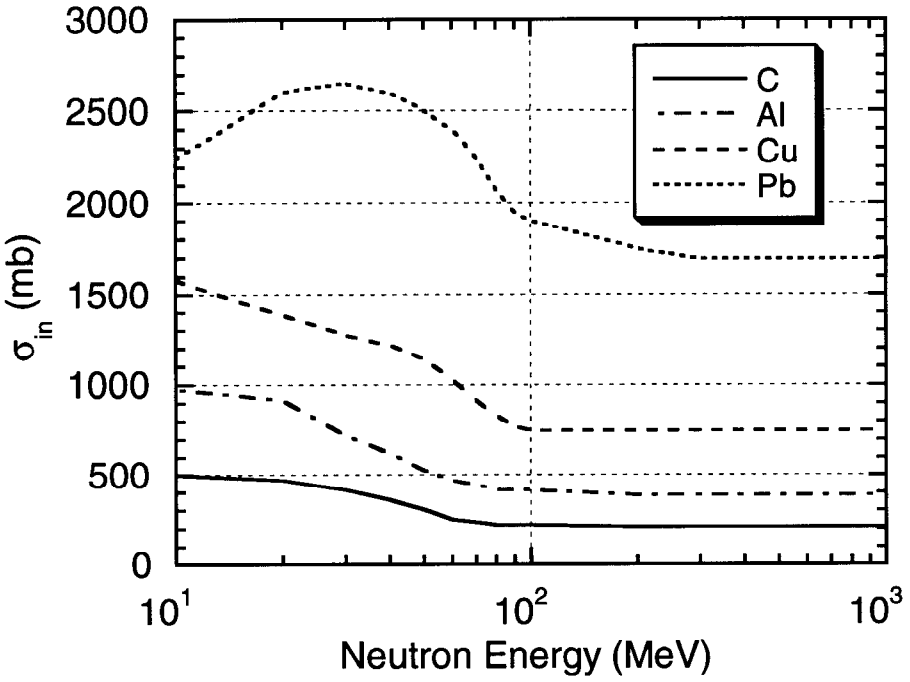

Fig. 3.2 Inelastic neutron cross sections as a function of energy in the range 1 to 1000 MeV. [Adapted from (Li61).]

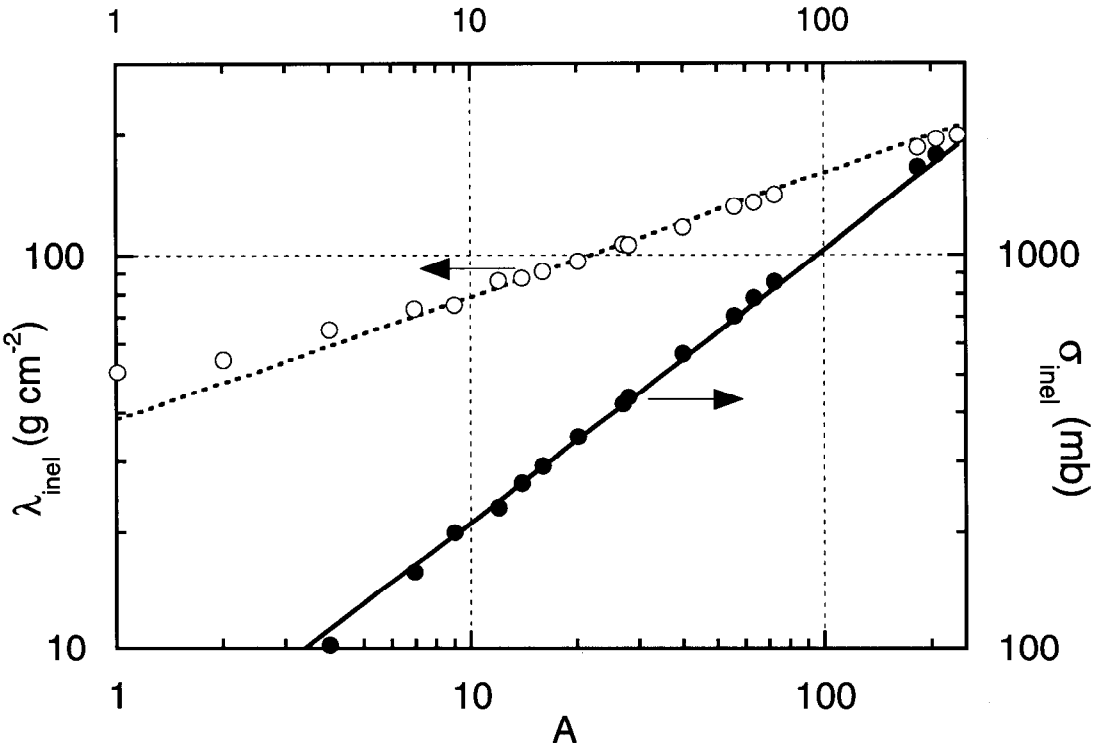

Fig. 3.3 Inelastic mean free path and cross section as a function of mass number. [Adapted from (Pa73).]

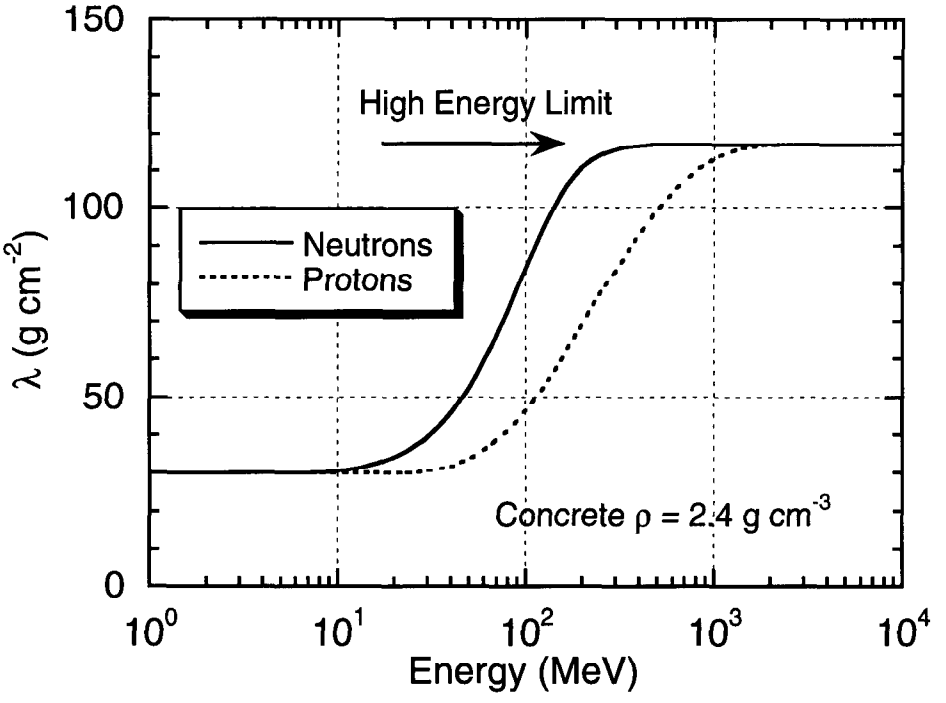

Fig. 3.4 The variation of the attenuation length λ for monoenergetic neutrons and protons in concrete as a function of neutron energy. The high energy limit is 117 g cm^{-2}. [Adapted from (Th88).]

III. Intermediate and High Energy Shielding-The Hadronic Cascade

The hadronic cascade from a conceptual standpoint

The cascade is initiated at proton accelerators when the beam interacts with components to produce neutrons and other particles. It can also arise at electron accelerators since, as described in Chapters 1 and 2, high energy secondary hadrons are produced in such circumstances.

The collision of a high energy nucleon with a nucleus produces a large number of particles; pions, kaons, and other nucleons as well as fragments of the struck nucleus. According to Thomas and Stevenson, above 1 GeV and at forward angles, the pions, protons, and neutrons, can be nearly equal in number (Th88). The neutrons may be classified as either **evaporation neutrons** or **cascade neutrons**. Evaporation neutrons originate as decays from excited states of residual nuclei and average a few MeV in energy. These neutrons tend to be isotropically distributed. Cascade neutrons are emitted by direct impact and their spectrum extends in energy up to the incident energy with diminishing probability following a spectrum roughly characterized as having an energy dependence proportional to *1/E*.

As the proton kinetic energy increases, other particles, notably $\pi^{\pm}$ and $K^{\pm}$, play roles in the cascade when their production becomes energetically possible. They are absorbed with absorption lengths comparable in magnitude to, but not identical with those of protons. These particles also decay into muons. Because of their long ionization ranges and lack of nuclear interactions, muons provide a pathway for energy to escape the cascade.

Hadrons, principally nucleons, with $E_o > 150$ MeV propagate the cascade. This is clear from the attenuation lengths shown in Fig. 3.2. Nucleons in the range $20 < E_n < 150$ MeV also transfer their energy predominantly by nuclear interactions but their energy gets distributed over many particles of all types energetically possible. The charged particles produced in such cascades are generally ranged-out in material or create yet other particles in the cascade. The role played by the energy of approximately 150 MeV for hadronic cascades is similar in kind to that of the critical energy for electromagnetic ones.

Neutral pions (π^o) are produced when the kinetic energy of the incident proton significantly exceeds the pion rest energy. The π^o rest energy is 134.9 MeV, its meanlife $\tau = (8.4 \pm 0.6) \times 10^{-17}$s with, thus, $c\tau = 25.2$ nm. The principal decay (99 % branching ratio) is into two γ-rays. An energetic π^o thus "appears" as two forward-peaked photons each with half of the π^o's total energy. The decay photons from π^o decay readily initiate electromagnetic cascades along with the hadronic one. It is possible for the electromagnetic channel to feed back into the hadronic cascade because it, too, produces high energy hadrons. However this effect is generally of little importance and, for most shielding calculations, the electromagnetic component of a hadronic cascade can be ignored. The exceptions principally involve energy deposition calculations at forward

angles (small values of θ). In fact, at hundreds of GeV, electromagnetic cascades dominate the energy deposition at forward angles. This feature can have important ramifications if one needs to consider radiation damage to equipment and the heat load on cryogenic systems.

In general, the neutrons are the principal drivers of the cascade because of the ionization energy loss for pions and for protons below 450 MeV where the ionization range becomes roughly equal to the interaction length. Also, any magnetic fields that are present which can deflect and disperse the charged particles present will not, of course, affect the neutrons. Furthermore, neutrons can be produced at large values of θ compared with the forward-peaked pions. These phenomena, in general, apply also to ions heavier than the proton with suitable corrections (especially at low energies) for nuclear structure effects. Scaling of proton results for heavier ions will, in general, roughly be according to the specific energy (MeV/amu). Figure 3.5 due to Torres (To96) is a schematic flow chart of the hadronic cascade process.

A simple one-dimensional cascade model

A simple one-dimensional model of the hadronic cascade was first proposed by Lindenbaum (Li61) and later augmented by Thomas and Stevenson (Th88). This approach gives instructive results and supplies some "intuition" into the nature of the hadronic cascade. Figure 3.6 defines the geometry. Suppose one initially has N_o incident high energy nucleons. After an individual collision, one of them continues in its original direction at a reduced energy but with the same attenuation length, λ or will generate one or more secondary particles also also with the same λ. The value of λ is approximately constant due to the limiting attenuation at high energy. This process continues until a number of collisions, n, have occurred which are sufficient to degrade the particle energies to approximately 150 MeV, below which energy the inelastic cross sections greatly increase (see Fig. 3.2). At this point a given particle is said to be removed from the cascade. For simplicity, it is assumed that n is an integer when, in reality, it has a statistical distribution. Thus, referring to the Fig. 3.6, the number ν_1 that reach $x = z$ having made no collisions is

$$\nu_1 = N_0 \exp(-z/\lambda) . \tag{3.9}$$

Suppose that there is one collision between 0 and z. The number that reach z is given by the product of the number that reach elemental coordinate dr multiplied by the probability of subsequently reaching z, times the probability of interacting in dr (dr/λ), times the multiplicity, m_1, in the first interaction. Integrating over dr:

$$\int_0^z \left[N_0 \exp\{-r/\lambda\}\right]\left[\exp\{-(z-r)/\lambda\}\right]\left[m_1 \frac{dr}{\lambda}\right] = \left(N_0 m_1 \frac{z}{\lambda}\right)\exp(-z/\lambda) = \nu_2 . \tag{3.10}$$

Now suppose there are two collisions. The number that reach z is the product of those that reach s having made one collision, multiplied by the probability of subsequently reaching z, times the multiplicity in the second interaction m_2, times the probability of interacting in ds:

$$\int_0^z \left[N_0 m_1 \frac{s}{\lambda} \exp\{-s/\lambda\} \right] \left[\exp\{-(z-s)/\lambda\} \right] \left[m_2 \frac{ds}{\lambda} \right] =$$

$$\left(N_0 m_1 m_2 \frac{z}{\lambda^2} \right) \exp(-z/\lambda) \int_0^z s\,ds = \left(N_0 m_1 m_2 \frac{z^2}{2\lambda^2} \right) \exp(-z/\lambda) = v_3 \qquad (3.11)$$

Therefore, with n defined as above, one can write:

$$N_n(x) = N_0 \beta_n (z/\lambda) \exp(-z/\lambda) \qquad (3.12)$$

where β is a "buildup" factor,

for $n = 1$ $\quad N_1 = v_1 \quad$ $\beta_1 = 1$

for $n = 2$ $\quad N_2 = v_1 + v_2 \quad$ $\beta_2 = 1 + (m_1 z/\lambda)$

for $n = 3$ $\quad N_2 = v_1 + v_2 + v_3 \quad$ $\beta_3 = 1 + (m_1 z/\lambda) + (m_1 m_2 z^2/2\lambda^2)$.

For arbitrary n, $$\beta_n = 1 + \frac{m_1 z}{\lambda} + \frac{m_1 m_2 z^2}{2\lambda^2} + \ldots + \frac{1}{n!} \left(\frac{z^n}{\lambda^n} \right) \prod_{i=1}^{n} m_i \qquad (3.13)$$

Thus this buildup factor is a monotonically increasing function of z. If $m_1 = m_2 = \ldots = m$ (i.e., one assumes that the multiplicity stays the same for all interactions in this simple model) and n is large, comparison with the series expansion of the exponential function reveals that β_n approximates an exponential dependence on z. The condition on n implies that the shield must be quite thick. The general result is that the attenuation length of the cascade, λ_{cas}, is somewhat larger than the value of the interaction length, λ, for a single interaction. Figure 3.7 is a plot of the number of particles after three generations as a function of x/λ ($m = 2$ and $n = 3$). The exponential region is not completely achieved until $z/\lambda \approx 10$. In concrete, this represents a depth of approximately 1200 g/cm^2. Figure 3.7 compares this estimate with data from an experimental measurement of Citron, et al. (Ci65) obtained in an experiment with 19.2 GeV/c protons incident on an iron slab which approximated the conditions on m and n mentioned above. Analytical approaches such as this one are constructive qualitatively but have severe limitations, among which are:

the restriction to one dimension,
the neglect of ionization energy losses and escape of energy carried by muons,
the neglect of elastic and multiple Coulomb scattering,
the assumption that <u>all</u> secondary particles go forward,
the assumption that multiplicities are <u>not</u> dependent on energy and particle type,
the assumption that λ is a constant for all particles at all energies, and
the neglect of radiative and electromagnetic cascade effects.

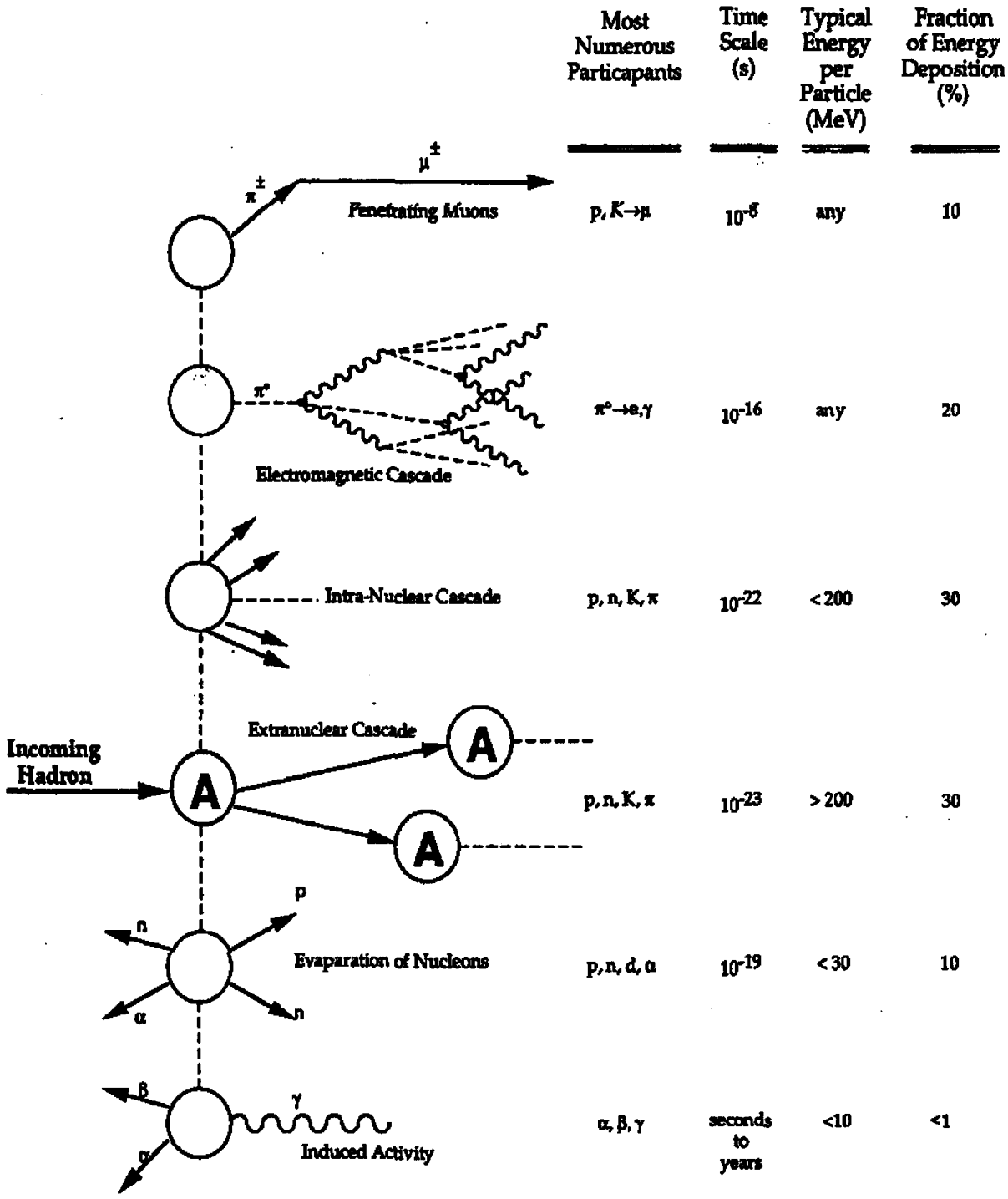

Fig. 3.5 Schematic representation of the development of the hadronic cascade and the major participants in any given path. The approximate time scales, the typical energies, and the fraction of energy deposition due to these participants are also shown. [Reproduced from Torres (To96).]

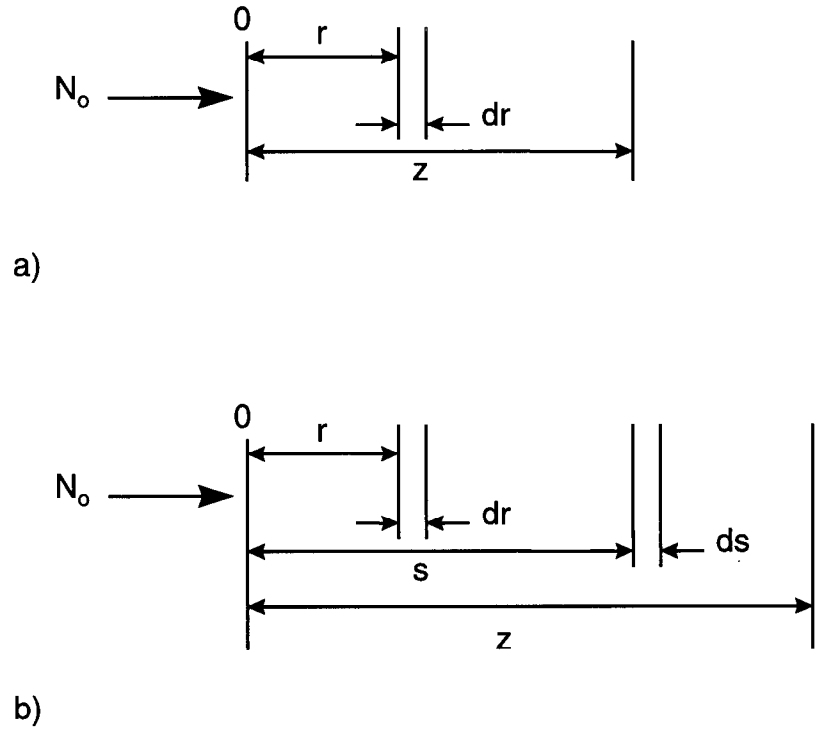

Fig. 3.6 a) Single collision geometry for the Lindenbaum approximation. b) Two collision geometry for the Lindenbaum approximation. [Adapted from (Th88).]

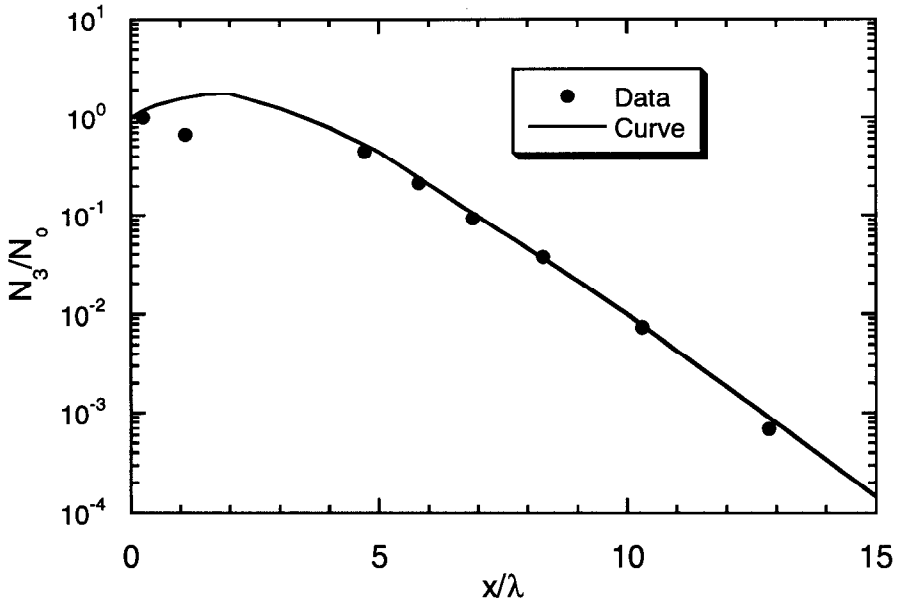

Fig. 3.7 Development of a one-dimensional cascade in the Lindenbaum approximation with $n = 3$ and $m = 2$ from Thomas and Stevenson (Th88) which is labeled "curve" compared with the laterally integrated star density in nuclear emulsions produced by a 19.2 GeV/c proton beam incident on an iron slab measured by Citron et al. (Ci65) which is labeled "data".

Semiempirical method: The Moyer model for point source

A number of references in the bibliography to this chapter (Pa73, IC78, Sc90, Ro76, St82, Th84, McC87, Te83, Te85, McC85, Co82a, and Co85) bear on the development of this model which is based, predominantly, on an exponential approximation with constants fitted to actual data spanning the range of proton beam energies from 7.4 to 800 GeV. The summary of this method here is largely taken from Patterson and Thomas (Pa73) and Schopper et al.(Sc90). This so-called "Moyer Model" was first developed by B. J. Moyer to solve particular shielding problems related to the Bevatron at the Lawrence Radiation Laboratory. The model predates the development of large, fast computers and advanced Monte-Carlo techniques but is still useful as means of checking more elaborate calculations.

The starting point is Fig. 3.8 that describes a "point" target source. The Moyer Model is developed as follows. The number of neutrons, *dN/dE* which are emitted into a given element of solid angle $d\Omega$ at angle θ relative to a target struck by N_p protons in an energy interval $E + dE$ is given by:

$$\frac{dN}{dE} = N_p\left(\frac{d^2Y}{dEd\Omega}\right)d\Omega B(E)\exp\left(-\frac{d\csc\theta}{\lambda(E)}\right) \quad , \tag{3.14}$$

where $B(E)$ is a "buildup factor" and the exponential function accounts for the attenuation of the radiation field by shielding of thickness, d, at the angle θ. The role of the double differential of the yield is obvious. In the above, the flux density at coordinates (r,θ) can be obtained by including the factor:

$$\frac{d\Omega}{dA} = \frac{1}{(a+d)^2\csc^2\theta} = \frac{1}{r^2\csc^2\theta} = \frac{1}{r'^2}, \tag{3.15}$$

The total flux density, ϕ, at the point where the ray emerges from the shield is given by

$$\phi = \frac{N_p}{r'^2}\int_{E_{\min}}^{E_{\max}} dE\ \frac{d^2Y}{dEd\Omega}B(E)\exp\left(-\frac{d\csc\theta}{\lambda(E)}\right). \tag{3.16}$$

Moyer introduced the following simplifying assumptions for this model. They are as follows:

A. $\lambda(E) = \lambda$ = constant for $E \geq 150$ MeV and $\lambda(E) = 0$ for $E < 150$ MeV. This is a simplified rendering of the leveling-off of the inelastic cross section at high energy. Thus,

$$\phi(E_n > 150\text{ MeV}) = \frac{N_p}{r'^2}\exp\left(-\frac{d\csc\theta}{\lambda}\right)\int_{150\text{MeV}}^{E_{\max}}\frac{d^2Y}{dEd\Omega}B(E)dE\,. \tag{3.17}$$

B. The neutrons emitted at angle θ can be represented by a simple function $f(\theta)$ multiplied by a multiplicity factor $M(E_{max})$ that depends only on the incident energy, thus:

$$\phi(E_n > 150 \text{ MeV}) = \frac{N_p}{r'^2}\exp\left(-\frac{d\csc\theta}{\lambda}\right)M(E_{\max})f(\theta) = \frac{N_p}{r'^2}\exp\left(-\frac{d\csc\theta}{\lambda}\right)g(E_{\max},\theta) \tag{3.18}$$

where $g(E_{\max},\theta)$ is an angular distribution function that is constant for a given value of $E_{\max}$ and for a particular target.

C. The dose equivalent per fluence, P, for neutrons is not strongly dependent on energy over a rather wide energy range near $E \approx 150$ MeV (see Fig. 1.5). Thus the dose equivalent just outside of the shield due to neutrons with $E > 150$ MeV can be taken to be $H(E_n > 150 \text{ MeV}) \approx P_{150}\,\phi(E_n > 150 \text{ MeV})$, where P_{150} is the value of this conversion factor at 150 MeV.

The total dose equivalent, H, is, then, given by

$$H = kH(E_n > 150 \text{ MeV}) \quad \text{where } k \geq 1. \tag{3.19}$$

This implicitly assumes that the low-energy neutrons are in equilibrium with those with $E > 150$ MeV so that the spectrum no longer changes with depth. This is a valid assumption for a shield more than a few mean free paths thick. Thus, Moyer's assumptions lead to:

$$H = \frac{kP_{150}N_p g(E_{\max},\theta)}{(a+d)^2\csc^2\theta}\exp\left(-\frac{d\csc\theta}{\lambda}\right). \tag{3.20}$$

One can generalize the results for the geometry shown in Fig. 3.8 with multiple materials in the shield. The parameter ζ is introduced to take care of the n multiple shielding components:

$$\zeta = \sum_{i=1}^{n}\frac{x_i}{\lambda_i}, \tag{3.21}$$

where the sum is over the n layers of shielding.

Stevenson et al. (St82) and Thomas and Thomas (Th84), have determined from global fits to data over a wide domain of energy that $f(\theta)$ is given by:

$$f(\theta) = \exp(-\beta\theta), \tag{3.22}$$

and that, in fact, $\beta \approx 2.3$ rad^{-1} (for $E_n > 150$ MeV).

Thus;

$$H = \frac{H_0(E_p)\exp(-\beta\theta)\exp(-\zeta\csc\theta)}{[r\csc\theta]^2} \qquad \text{in which} \qquad (3.23)$$

$$r = a + \sum_{i=1}^{n} x_i$$

and where $H_o(E_p)\exp(-\beta\theta)$ is determined from the yield data and empirical measurements. $H_O(E_p)$ is best fit as a power law; $H_O(E_p) = kE^n$. From such results, per incident proton:

$$H_o(E_p) = [(2.84 \pm 0.14) \times 10^{-13}]\, E_p^{(0.80 \pm 0.10)} \qquad (\text{Sv m}^2)$$

$$= 2.84 \times 10^{-8}\, E_p^{0.8} \ (\text{mrem m}^2) = 2.8 \times 10^{-4}\, E_p^{0.8} \ (\text{mrem cm}^2), \qquad (3.24)$$

with E_p in GeV. These results are derived for relatively "thick" targets (like accelerator magnets) in tunnel configurations. Schopper et al. (Sc90), based on Monte-Carlo results gives values for "thin" targets of $k = 2.0 \times 10^{-14}$ (Sv m^2) and $n = 0.5$. A beam pipe would be an example of a "thin" target. The variations thus reflect buildup in the shower. For thick lateral shields close to the beam where the cascade immediately becomes fully developed and self-shielding arises, $k = (6.9 \pm 0.1) \times 10^{-15}$ (Sv m^2) and $n = 0.8$ independent of target material [(Sc90) and(St87)].

Similarly, recommended values of λ are for concrete and other materials as a function of mass number A;

concrete:	1170 ± 20 kg/m^2	$= 117$ g/cm^2
others:	$428A^{1/3}$ kg/m^2	$= 42.8A^{1/3}$ g/cm^2.

These values are 15-30% larger than the "nuclear interaction lengths" and are reflective of the shower phenomena illustrated by the one-dimensional Lindenbaum model.

If one sets the partial derivative, $\partial H / \partial\theta$, to zero, one can derive an equation for determining the value of $\theta = \theta'$ at which the maximum dose equivalent occurs. Generally this equation can be solved by successive approximation methods,

$$\zeta\cos\theta' - \beta\sin^2\theta' + 2\cos\theta'\sin\theta' = 0. \qquad (3.25)$$

One can substitute into the above equation to get the maximum dose equivalent at a given radial depth. According to McCaslin (McC87), with r in meters and over a wide range of values of ζ, the following holds:

$$H_{\max} = 1.66\times10^{-14} E_p^{0.8} \exp(-\zeta)\frac{\zeta^{0.245}}{r^2} \quad (\text{Sv per incident proton}). \qquad (3.26)$$

For values of $\zeta > 2$, the following is an equally accurate approximation:

$$H_{\max} = 1.26\times10^{-14} E_p^{0.8} \frac{\exp(-1.023\zeta)}{r^2} \text{ (Sv per incident proton).} \qquad (3.27)$$

The Moyer Model for line sources

Assume a uniform source of one proton interacting per unit length. Then, the dose equivalant from the individual increments along the line source contribute to the total at any given point, P, external to the shield. Fig. 3.9 shows the integration variables. One can integrate the elements $d\ell$ of a line source at given perpendicular distance r as follows. Making the change of variable of intregration from the line integral the integral over angle θ, $d\ell = r\csc^2\theta d\theta$;

$$H = H_0(E_p)\int_{-\infty}^{\infty} d\ell \frac{\exp(-\beta\theta)\exp(-\zeta\csc\theta)}{r^2\csc^2\theta} =$$

$$H_0(E_p)\int_0^{\pi} d\theta r\csc^2\theta \frac{\exp(-\beta\theta)\exp(-\zeta\csc\theta)}{r^2\csc^2\theta} =$$

$$\frac{H_0(E_p)}{r}\int_0^{\pi} d\theta\exp(-\beta\theta)\exp(-\zeta\csc\theta) = \frac{H_0(E_p)}{r} M(\beta,\zeta)$$

(per interacting proton per unit length). (3.28)

The integral in the above, $M(\beta,\zeta)$, is known as the **Moyer integral**. The values of this integral have been tabulated by Routti and Thomas (Ro76). In view of the above results, $M(2.3,\zeta)$ has obvious special significance and is tabulated extensively by, e.g., Schopper et al. (Sc90). Tesch (Te83) made an important contribution in that he determined an approximation to this integral that has become called the "Tesch approximation":

$$M_T(2.3,\zeta) = 0.065\exp(-1.09\zeta). \qquad (3.29)$$

For "intermediate" values of ζ, $M_T(2.3,\zeta)$ can be used instead of $M\ (2.3,\zeta)$ to simplify calculations. Table 3.2 gives the ratio $M_T(2.3,\zeta)/M\ (2.3,\zeta)$ as a function of ζ. Of course, few so-called "line sources" are actually infinite in length. Thus, the integration can be limited to a finite angular range. Likewise, only a limited angular range (and hence length) contributes significantly to the Moyer integral. Tables 3.3 and 3.4 taken give angular integration limits (in degrees) corresponding to 90 % of the $M\ (2.3,\zeta)$ as a function of ζ (Table 3.3) and the distances along the z-axis corresponding to 90 % of $M(2.3,\zeta)$ as a function of the radial distance and ζ (Table 3.4). These calculations were done for concrete shields. McCaslin (McC85) demonstrated that the Moyer Model approach is effective for moderately energetic heavy ions. It has also been found that the Moyer Model approach works well even into the intermediate energy region $200 < E_o <$ 1000 MeV. This may be interpreted as due to the relatively smooth dependence of

neutron yield upon incident proton kinetic energy. The Moyer Model generally does not work at forward angles. For these situations, the Boltzmann equation must be solved. Monte-Carlo calculations are often the best approximation to such solutions.

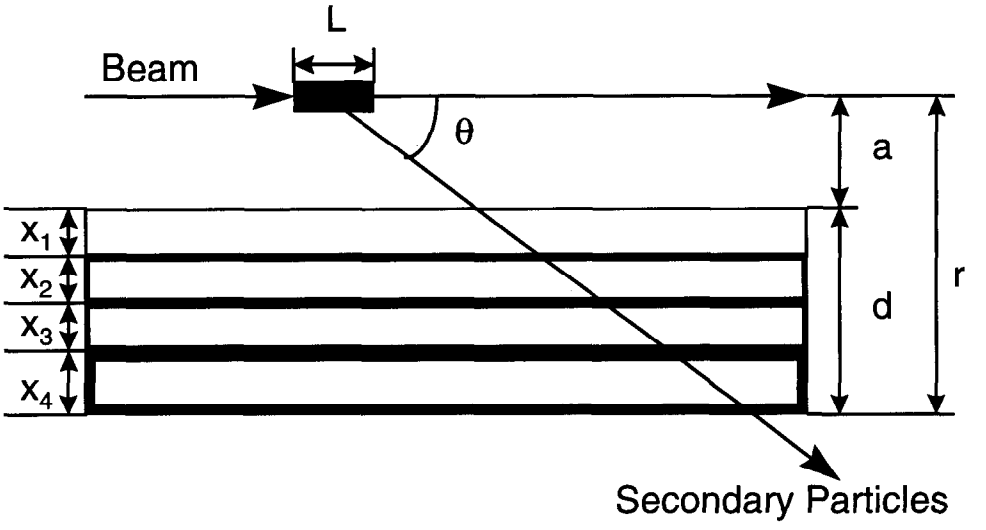

Fig. 3.8 Sketch of the geometry for the empirical Moyer Model. The proton beam, N_p impinges on the target of length L. The shield materials represented by the layers X_i, could be, for example, iron, concrete, earth and air respectively. a is the internal radius of the tunnel. The observer is situated at a radial thickness of d equal to the sum of the thicknesses of the four layers.

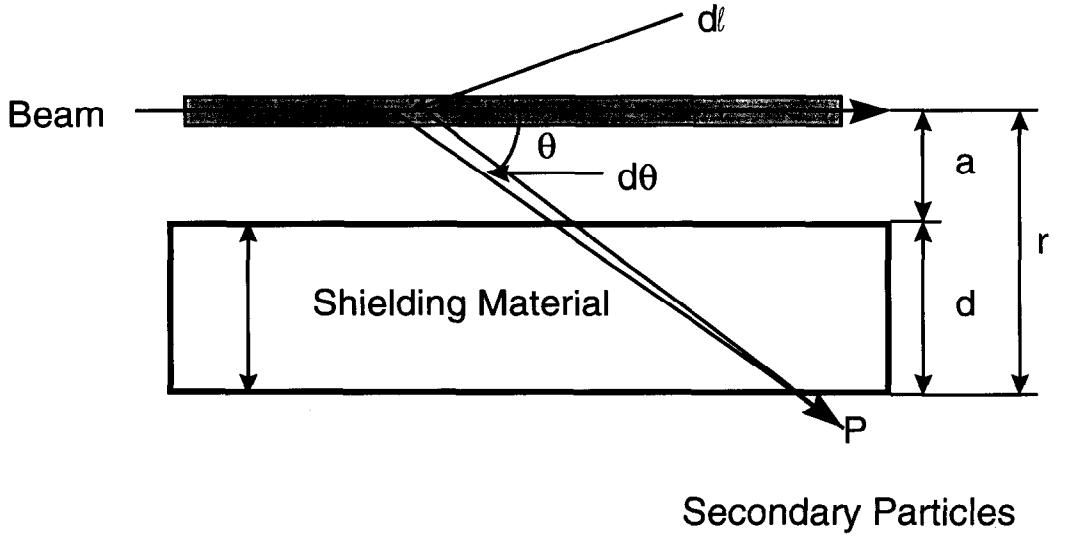

Figure 3.9 Variables of integration of Moyer point source result needed to obtain Moyer line source results.

Table 3.2 Values of the Ratio $M_T(2.3,\zeta)/M(2.3,\zeta)$ as a function of ζ. [Adapted from (Sc90).]

ζ	$M_T(2.3,.\zeta)/M(2.3/\zeta)$	ζ	$M_T(2.3,.\zeta)/M(2.3/\zeta)$
0.2	0.27	11	1.02
1	0.53	12	0.99
2	0.75	13	0.95
3	0.90	14	0.91
4	1.00	15	0.86
5	1.06	16	0.82
6	1.09	17	0.78
7	1.10	18	0.73
8	1.10	19	0.69
9	1.08	20	0.65
10	1.06		

Table 3.3 Angular integration limits in degrees which contain 90% of the Moyer Integral $M(2.3,\zeta)$. [Adapted from (Sc90).]

ζ	Lower Limit	Upper Limit	ζ	Lower Limit	Upper Limit
2.5	31.52	106.58	12	57.25	106.29
3	24.35	107.15	13	58.45	106.04
4	39.00	107.64	14	59.74	105.78
5	42.67	107.73	15	60.66	105.54
6	45.77	107.66	16	61.49	105.29
7	48.51	107.48	17	62.34	105.04
8	50.69	107.28	18	63.22	104.80
9	52.7	107.04	19	64.08	104.54
10	54.34	106.79	20	64.63	104.30
11	56.07	106.54			

Table 3.4 Distances corresponding to 90% limits in Moyer Integrals. [Adapted from (Sc90).]

Radial Distance (m)	Thickness (concrete) (meters)	Thickness (concrete) ζ	Upstream Limit, z_1 (meters)	Downstream Limit, z_2 (meters)	Total Length z_2-z_1 (meters)
1.5	0.5	1.0	-4.2	0.3	4.5
2.0	1.0.	2.0	-3.7	0.6	4.3
3.5	2.5	5.0	-3.8	1.1	4.9
6.0	5.0	10.0	-4.3	1.8	6.1
8.5	7.5	15.0	-4.8	2.4	7.2
11.0	10.0	20.0	-5.2	2.8	8.0

Review of Commonly Used Monte-Carlo Codes

HETC

This code, developed over many years under the leadership of R. G. Alsmiller at the Oak Ridge National Laboratory, is considered by some to be the benchmark hadron shielding code. It has been upgraded many times and can, in suitably augmented versions, follow particles from the 20 TeV region down to thermal energies. It is an extremely flexible code but has the important disadvantage that the individual events are written to mass storage. It is the responsibility of the user to write a program to analyze the results. In terms of CPU-time HETC is also relatively slow so that calculations to be done should be carefully selected. It is seen to be preferable to use selected HETC runs to calibrate some faster, but less accurate code. It has been described by Armstrong (Ar80) and Gabriel (Ga85). It now uses the same event generator used for FLUKA (see below). A simple example of an HETC calculation is given in Fig. 3.10 taken from Alsmiller's work (Al75) for the case of 200 MeV protons incident on "thin" and "thick" aluminum targets. It plots r^2H as a function of angle for several intervals of θ in a concrete shield.

FLUKA

FLUKA is an integrated, versatile multi-particle Monte Carlo program, capable of handling a wide variety of radiation transport problems. Its energy range extends from one keV (for neutrons, thermal energies) to thousands of TeV. FLUKA can simulate with a similar level of accuracy the propagation of hadronic and electromagnetic cascades, cosmic muons, slowing-down neutrons and synchrotron radiation in the keV region. An original treatment of multiple Coulomb scattering allows the code to handle accurately some challenging problems such as electron backscattering and energy deposition in thin layers. In a fully analog mode, FLUKA can be used in detector studies to predict fluctuations, coincidences and anti-coincidences; on the other hand, a rich supply of biasing options makes it well suited for studies of rare events, deep penetration and shielding in general. This code originated as high-energy particle transport code, developed by a CERN-Helsinki-Leipzig collaboration, principally by J. Ranft as discussed by Aarnio, et al. (Aa86). More recently, it has been completely rewritten and extended to low energies as discussed by Fassò et al. (Fa93). It handles more than 30 different particles, including neutrons from thermal energies to about 20 TeV and photons from 1 keV to thousands of TeV. Several biasing techniques are available. Recoil protons and protons from N(n,p) reaction are transported explicitly.

CASIM

A. Van Ginneken has developed this progam (Va75). It was designed to simulate the average behavior of hadrons in the region 10 to 1000 GeV and has been extended to 20 TeV (Va87) It uses inclusive production distributions directly in order to obtain the particles to follow. It uses the Hagedorn-Ranft thermodynamic model. Only one or two high energy particles are created in each collision and these carry a weight related to their

probability of production and the energy carried with them. Path length stretching and particle splitting have been introduced. Electromagnetic showers resulting from π^o production are calculated using AEGIS. Simple"standardized" geometries are available. However, the user generally writes a FORTRAN subroutine to set up the geometry of interest. This subroutine consists of "IF" statements used to deduce the location of the particle in space or in magnetic fields. The program readily allows magnetic fields to be used. A muon version called CASIMU (now MUSIM) has been written (Va87). The accuracy of the hadron version has been verified for energies up to 800 GeV (Co82a) and the muon version has been verified up to 800 GeV [production and transport in complicated shields, (Co89b)] and 500 GeV [transport in an earth shield (Co89a)]. Normally, CASIM is not set up to follow particles with momenta less than 300 MeV/c, which corresponds to a kinetic energy of 47 MeV for nucleons. All low energy phenomena, then, is obtained by matching energy spectra and fluence at this energy with results of codes capable of tracking lower energy particles (e.g., HETC, FLUKA, and MARS).

MARS

The MARS Monte Carlo code system has been developed over a number of years by N. Mokhov, et al. (Ka89, Mo95, and Kr97). The code allows fast inclusive simulation of three-dimensional hadronic and electromagnetic cascades for shielding, accelerator, and detector components in the energy range from a fraction of an electronvolt up to 100 TeV. The current version uses the phenomenological model for inclusive hadron- and photon-nucleus interactions for $E > 5$ GeV and exclusive cascade-exciton model at 1 MeV $< E <$ 5 GeV. It includes photo- and electro-production of hadrons and muons, improved algorithms for the 3-body decays, precise particle tracking in magnetic fields, synchrotron radiation by electrons and muons, significantly extended histogramming capabilities and material description, improved computational performance. In addition to the direct energy deposition calculations, a set of dose conversion per fluence factors for all particles including neutrinos[1] is built into the code. The code includes links to the MCNP4A code for neutron and photon transport below 20 MeV, to the ANSYS code for thermal and stress analyses and to the code for multi-turn particle tracking in large synchrotrons and collider rings. The geometry module allows a set of the pre-defined shapes, arbitrary user-defined 3-D description, or uses the object-oriented engine coupled with VRML/2.0 - the newly approved standard for a 3-D World Wide Web-oriented geometry description. This allows one to rely on a convenient VRML-enabled WWW browser for a navigation through the entire geometry, a link of the geometry description to the user Web page and a visualization of the output results with a possible scripting. The geometry module is linked to the object-oriented database for a fast storage/retrieving of complex geometries. The developments were induced by numerous challenging applications - Fermilab accelerator, detector and shielding upgrades, Large Hadron Collider machine and detector studies, muon colliders etc - as well as by a continuous desire to increase code reliability, flexibility and user friendliness.

[1] The dose equivalent per fluence for neutrinos is finite but very small and strongly energy dependent for neutrino energies between 10 MeV and 10 TeV (Co97).

General comments on Monte-Carlo star-to-dose conversions

All of the above codes, in general, calculate **star densities**. This quantity is more correctly called the density of inelastic interactions (stars/cm^3). The term "star" comes from historic cosmic ray work in which the high energy interaction events, with their large multiplicities, appeared as tracks originating from a point. The conversion factor from star densities to dose equivalent is rather important and has recently been calculated by Stevenson (St86). While this conversion factor is somewhat dependent upon the position in the shield, after reasonable shield thicknesses sufficient to establish "equilibrium" spectra a constant value may be used. For concrete a value of 4.9 x 10^{-8} Sv cm^3/star is obtained. These values are given in Table 3.5. This table also gives the **star fluence** obtained by multiplying by the nuclear interaction length. The star fluence roughly corresponds to the fluence of hadrons having energies above that where the cross section "levels off". As one can see, the energy dependence is rather weak.

Compilations of such calculations have been given by Van Ginneken (Va75 and Va87) and by Cossairt (Co82b). Schopper et al. (Sc90) have also compiled a comprehensive set of Monte-Carlo results. A convenient way to display these results is to provide contour plots of star density as function of longitudinal coordinate, *Z*, and radial coordinate, *r*, assuming cylindrical symmetry. Results for solid concrete and iron cylinders are provided in Figs. 3.11 and 3.12. Figures 3.13 and 3.14 provide results as a function of radius at the position of the longitudinal maximum and the variation of the dose equivalent on the longitudinal axis as a function of *z* for such shields. Obviously, many realistic situations are not covered adequately by limiting the calculations to such simple configurations. One of the salient advantages of the Monte-Carlo method is the ability to handle configurations of arbitrary complexity. Figure 3.15 display some examples of some typical results encountered in the shielding of high energy proton accelerators. In this set of figures, the outermost shield is always soil. In all of these plots, concrete, if present, was taken to have a density of 2.4 g cm^{-3}. Soil surrounding concrete shields and or beam pipes was taken to have a density of 2.24 g cm^{-3}.

Table 3.5 Coefficients to convert star densities S^* and star fluence ϕ^* into dose equivalent. A star density is transformed into star fluence by the relation $\phi^* = S^*\lambda'$ where λ' is the nuclear interaction length. [Adapted from (St86).]

Proton Energy (GeV)	Absorber Material	Conversion Sv cm^3/star (x 10^{-8})	λ' (cm)	Conversion Sv cm^2/star (x 10^{-9})
10	Iron	2.04 ± 0.06	17.1	1.19 ± 0.04
100	Iron	2.15 ± 0.08	17.8	1.21 ± 0.05
1000	Iron	2.12 ± 0.08	17.2	1.23 ± 0.05
Mean	Iron	2.10 ± 0.04		1.21 ± 0.02
100	Aluminum	4.62 ± 0.17	38.6	1.20 ± 0.04
100	Tungsten	1.19 ± 0.05	9.25	1.29 ± 0.05
	Concrete	4.9	40.0	1.22
Mean	All			1.22 ± 0.02

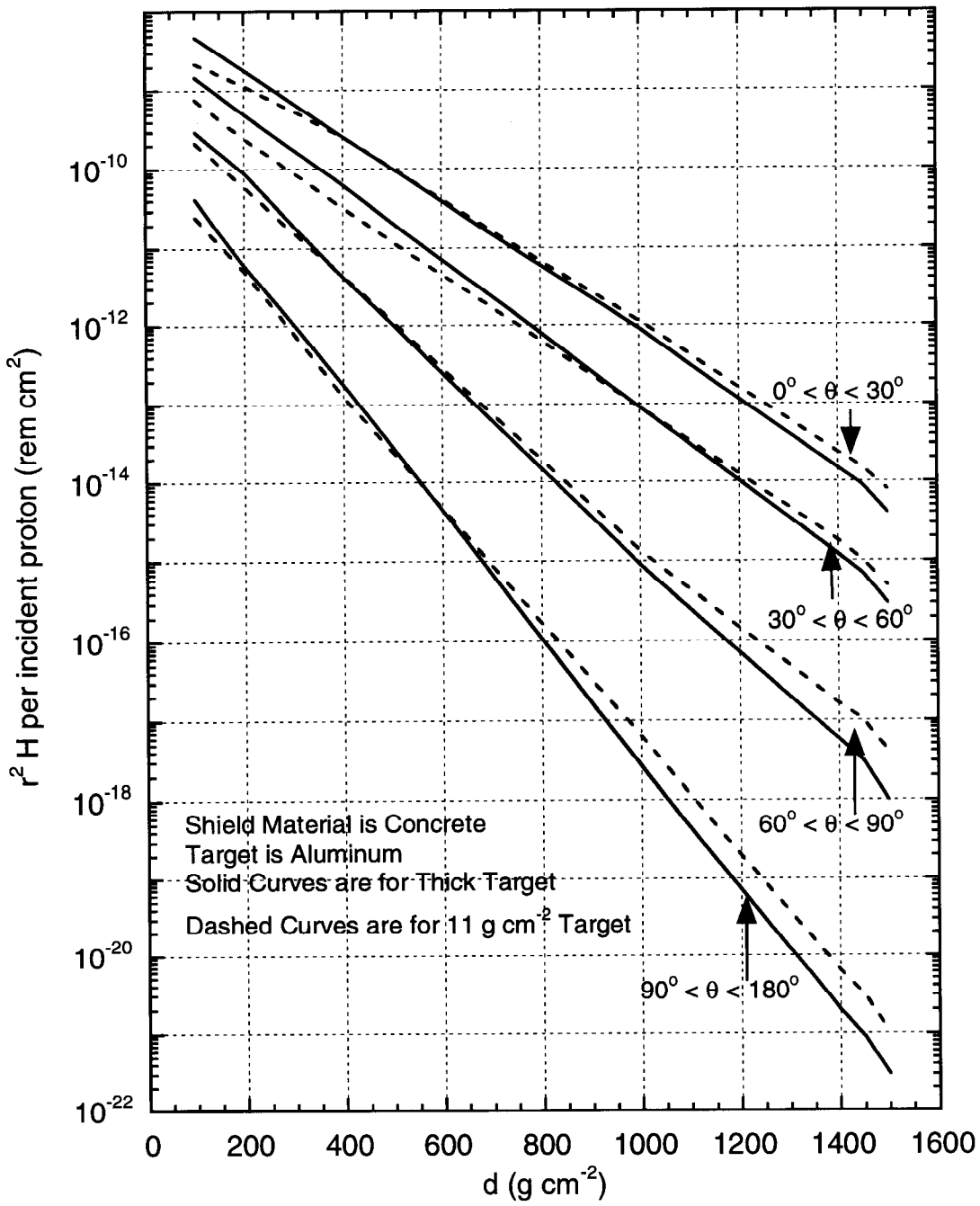

Fig. 3.10 HETC calculations of r^2H as a function of CONCRETE shield thickness, d, averaged over several intervals of θ for 200 MeV protons incident on an aluminum target. [Adapted from (Al75).]

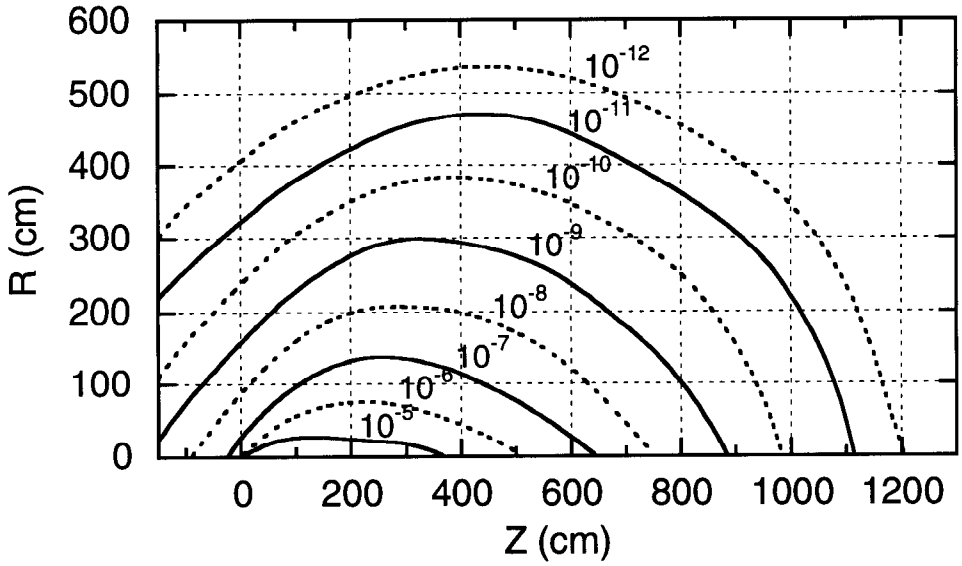

Fig. 3.11a Monte-Carlo results for 30 GeV/c protons incident on a CONCRETE cylinder (Va75). Contours of equal star density (stars cm^{-3}) per incident proton are plotted. The beam of 0.3 x 0.3 cm cross section is centered on the cylinder axis and starts to interact at zero depth. The star density includes only those due to hadrons above 0.3 GeV/c momentum. Contours of higher star density are not shown for clarity while those of lower star density are not included due to statistical uncertainty.

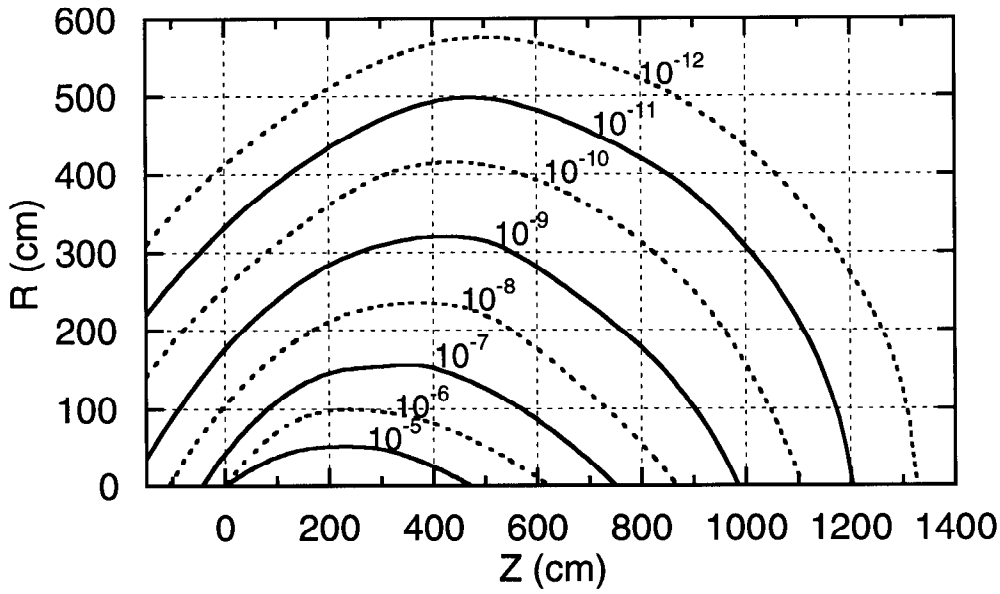

Fig. 3.11b Monte-Carlo results for 100 GeV/c protons incident on a CONCRETE cylinder (Va75). Contours of equal star density (stars cm^{-3}) per incident proton are plotted. The beam of 0.3 x 0.3 cm cross section is centered on the cylinder axis and starts to interact at zero depth. The star density includes only those due to hadrons above 0.3 GeV/c momentum. Contours of higher star density are not shown for clarity while those of lower star density are not included due to statistical uncertainty.

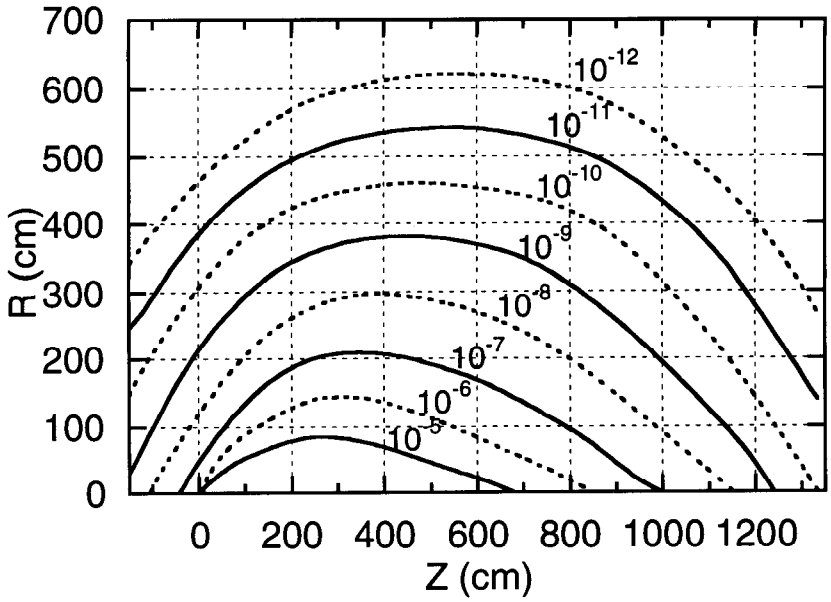

Fig. 3.11c Monte-Carlo results for 1 TeV/c protons incident on a CONCRETE cylinder (Va75). Contours of equal star density (stars cm^{-3}) per incident proton are plotted. The beam of 0.3 x 0.3 cm cross section is centered on the cylinder axis and starts to interact at zero depth. The star density includes only those due to hadrons above 0.3 GeV/c momentum. Contours of higher star density are not shown for clarity while those of lower star density are not included due to statistical uncertainty.

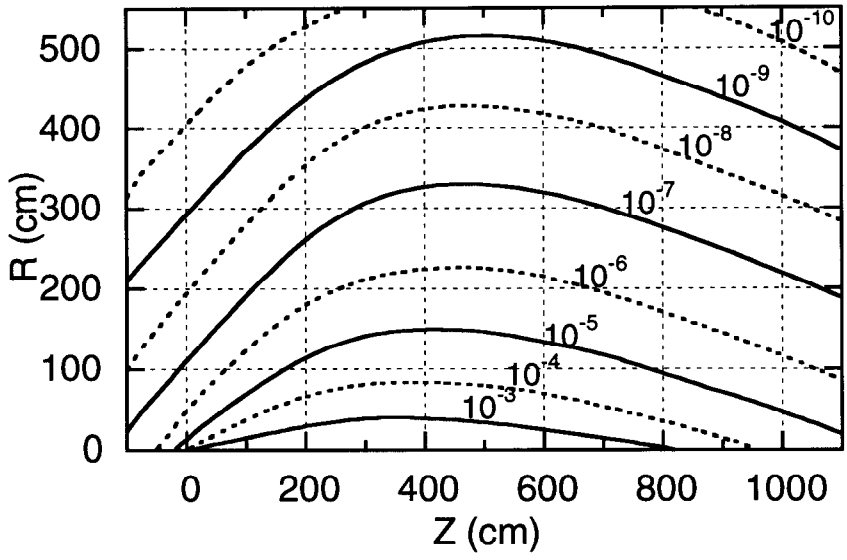

Fig. 3.11d Monte-Carlo results for 10 TeV/c protons incident on a CONCRETE cylinder (Va87). Contours of equal star density (stars cm^{-3}) per incident proton are plotted. The beam of 0.3 x 0.3 cm cross section is centered on the cylinder axis and starts to interact at zero depth. The star density includes only those due to hadrons above 0.3 GeV/c momentum. Contours of higher star density are not shown for clarity while those of lower star density are not included due to statistical uncertainty.

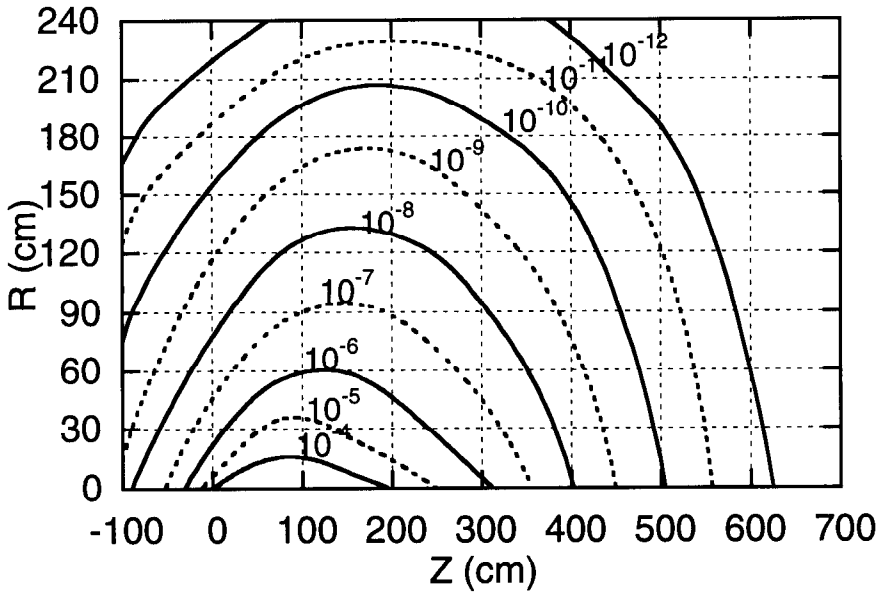

Fig. 3.12a Monte-Carlo results for 30 GeV/c protons incident on an IRONcylinder (Va75). Contours of equal star density (stars cm^{-3}) per incident proton are plotted. The beam of 0.3 x 0.3 cm cross section is centered on the cylinder axis and starts to interact at zero depth. The star density includes only those due to hadrons above 0.3 GeV/c momentum. Contours of higher star density are not shown for clarity while those of lower star density are not included due to statistical uncertainty.

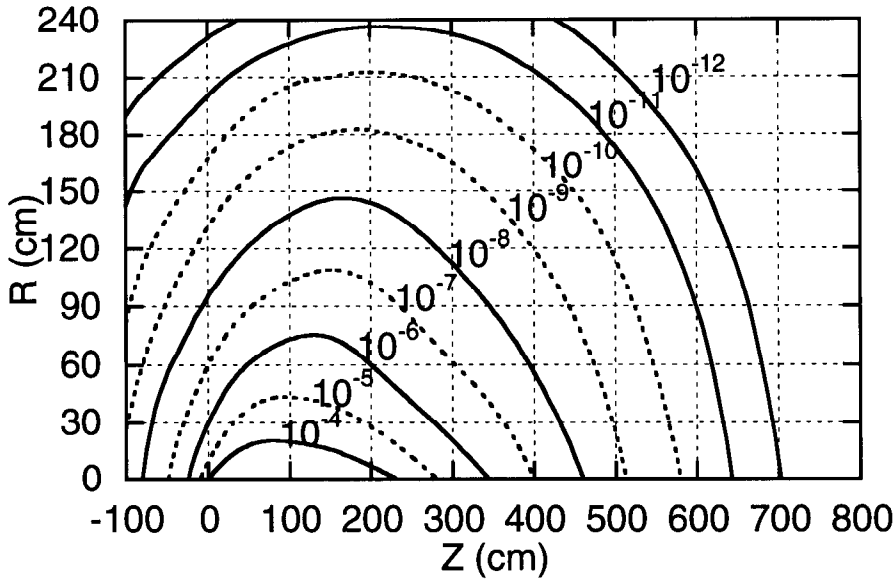

Fig. 3.12b Monte-Carlo results for 100 GeV/c protons incident on an IRON cylinder (Va75). Contours of equal star density (stars cm^{-3}) per incident proton are plotted. The beam of 0.3 x 0.3 cm cross section is centered on the cylinder axis and starts to interact at zero depth. The star density includes only those due to hadrons above 0.3 GeV/c momentum. Contours of higher star density are not shown for clarity while those of lower star density are not included due to statistical uncertainty.

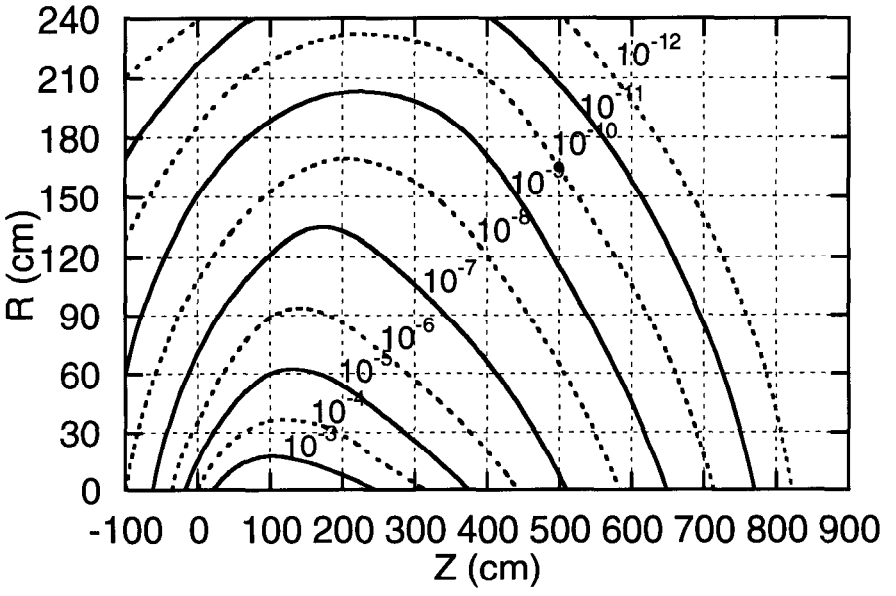

Fig. 3.12c Monte-Carlo results for 1 TeV/c protons incident on an IRON cylinder (Va75). Contours of equal star density (stars cm^{-3}) per incident proton are plotted. The beam of 0.3 x 0.3 cm cross section is centered on the cylinder axis and starts to interact at zero depth. The star density includes only those due to hadrons above 0.3 GeV/c momentum. Contours of higher star density are not shown for clarity while those of lower star density are not included due to statistical uncertainty.

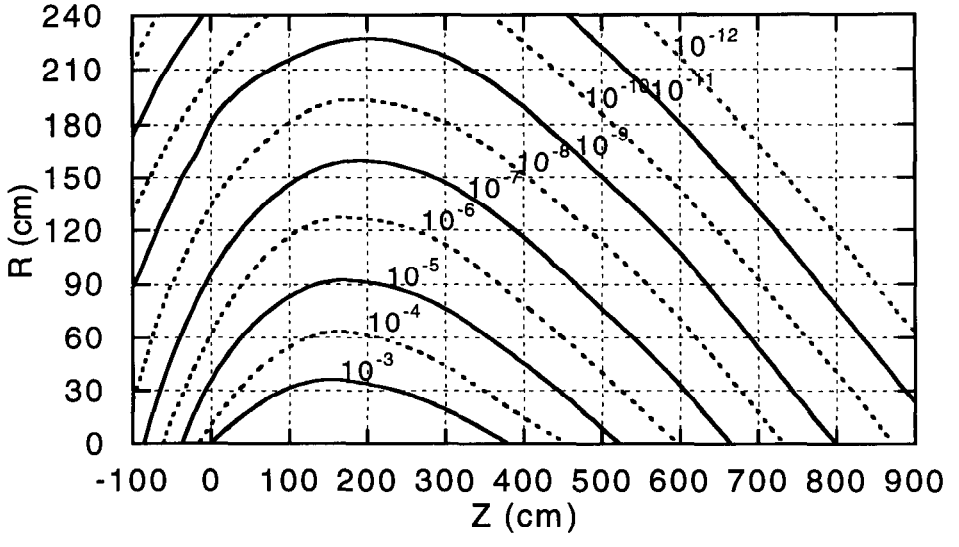

Fig. 3.12d Monte-Carlo results for 10 TeV/c protons incident on an IRON cylinder (Va87). Contours of equal star density (stars cm^{-3}) per incident proton are plotted. The beam of 0.3 x 0.3 cm cross section is centered on the cylinder axis and starts to interact at zero depth. The star density includes only those due to hadrons above 0.3 GeV/c momentum. Contours of higher star density are not shown for clarity while those of lower star density are not included due to statistical uncertainty.

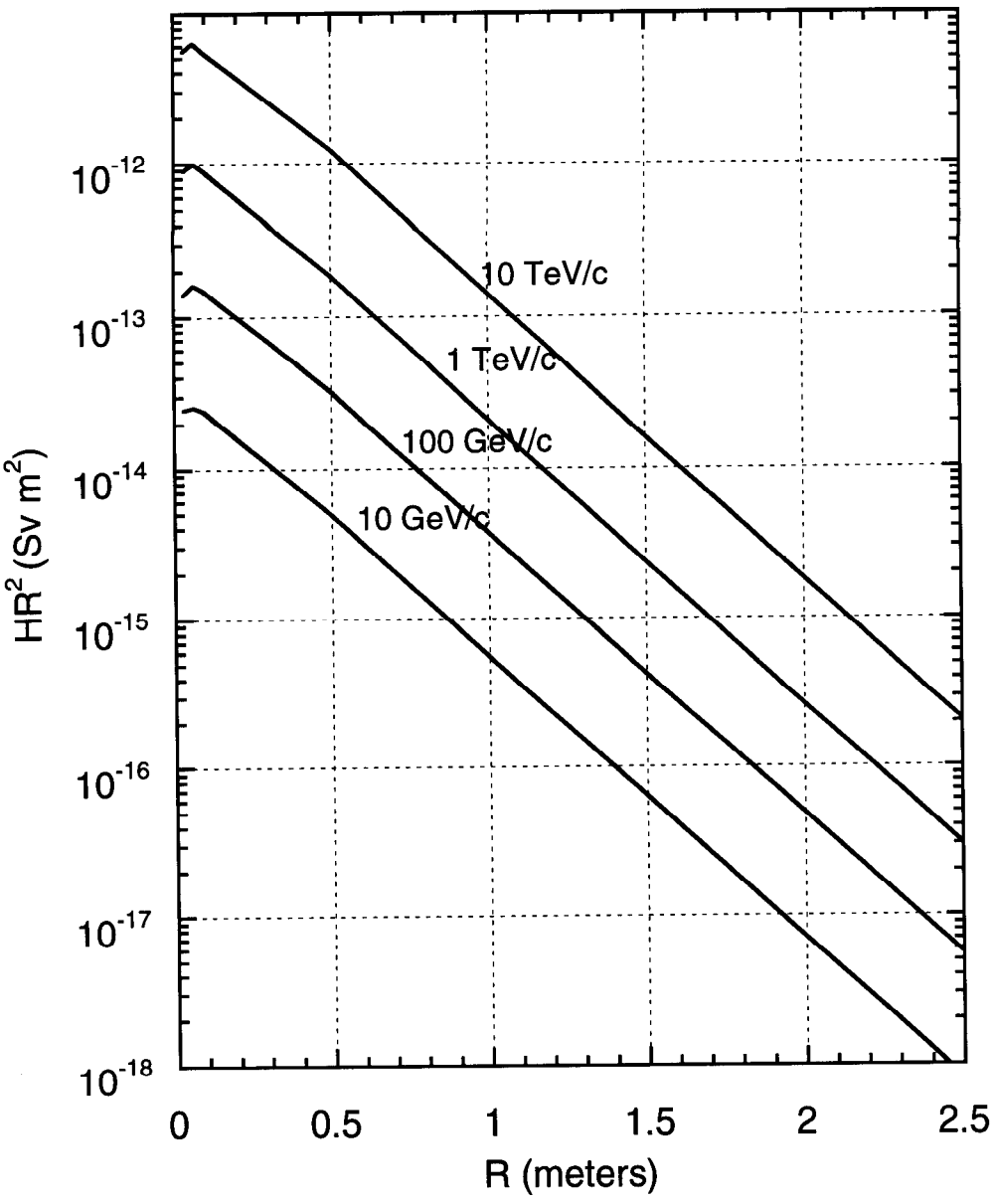

Fig. 3.13 Variation of the dose equivalent per proton at the position of the longitudinal maximum multiplied by the square of the radius HR^2 versus radius, R, for proton-induced cascades in IRON of density 7.2 g cm^{-3}. The results are fits to calculations obtained using FLUKA and MARS. [Adapted from (Sc90).]

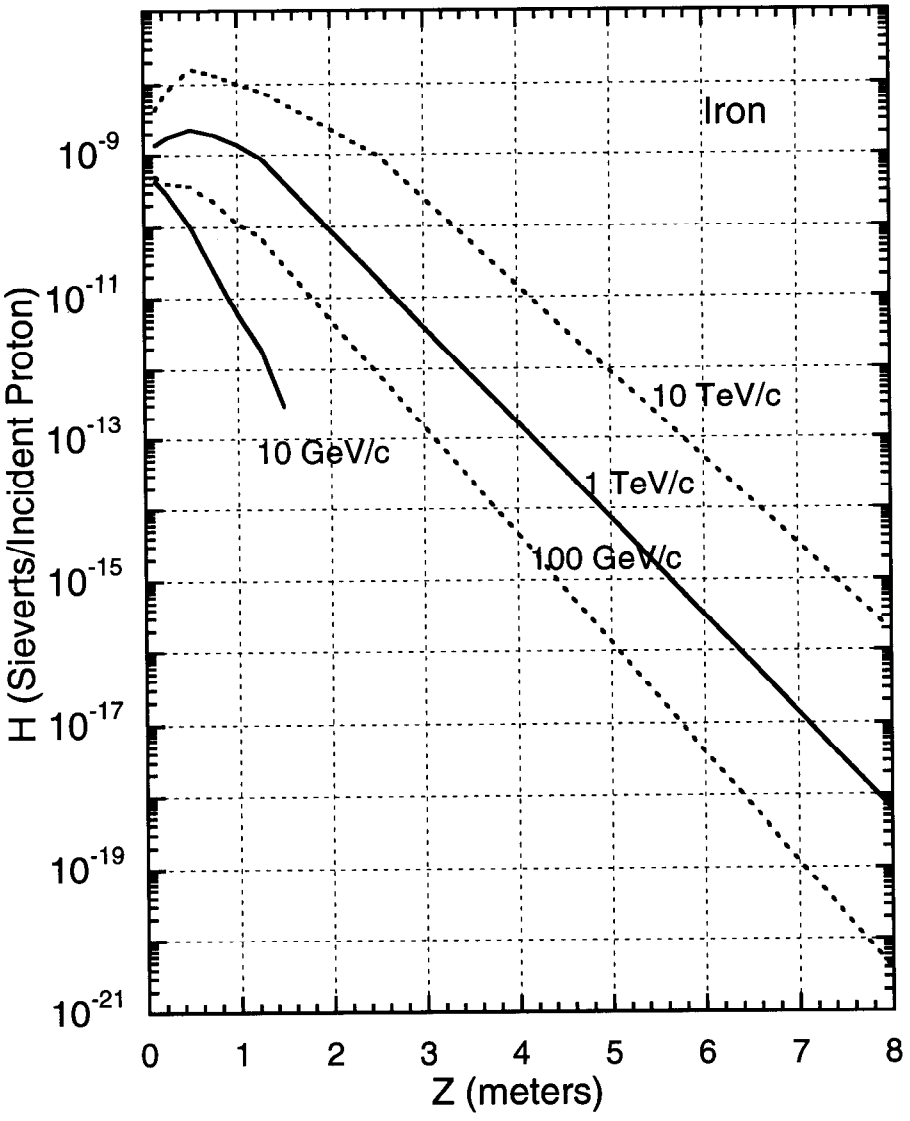

Fig. 3.14a Variations of the dose equivalent per proton, H, on the longitudinal axis vs. depth Z in the shield for proton-induced cascades in IRON of density 7.2 g cm^{-3}. The curves are the result of CASIM calculations for incident proton momenta of 100 GeV/c, 1 TeV/c, and 10 TeV/c and FLUKA results for 10 GeV/c. [Adapted from (Sc90).]

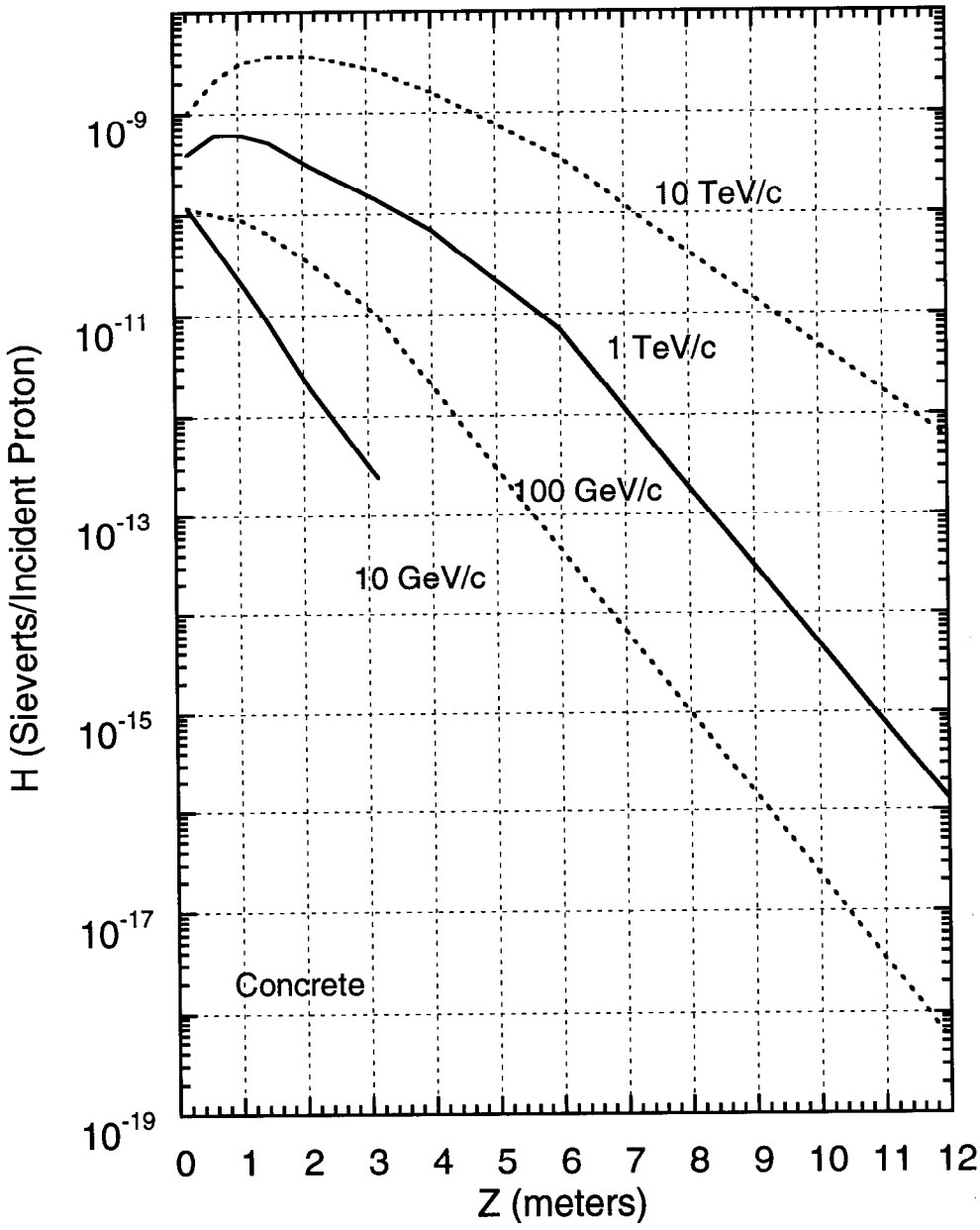

Fig. 3.14b Variations of the dose equivalent per proton, H, on the longitudinal axis vs. depth Z in the shield for proton-induced cascades in CONCRETE of density 2.4 g cm^{-3}. The curves are the result of CASIM calculations for incident proton momenta of 100 GeV/c, 1 TeV/c, and 10 TeV/c and FLUKA results for 10 GeV/c. [Adapted from (Sc90).]

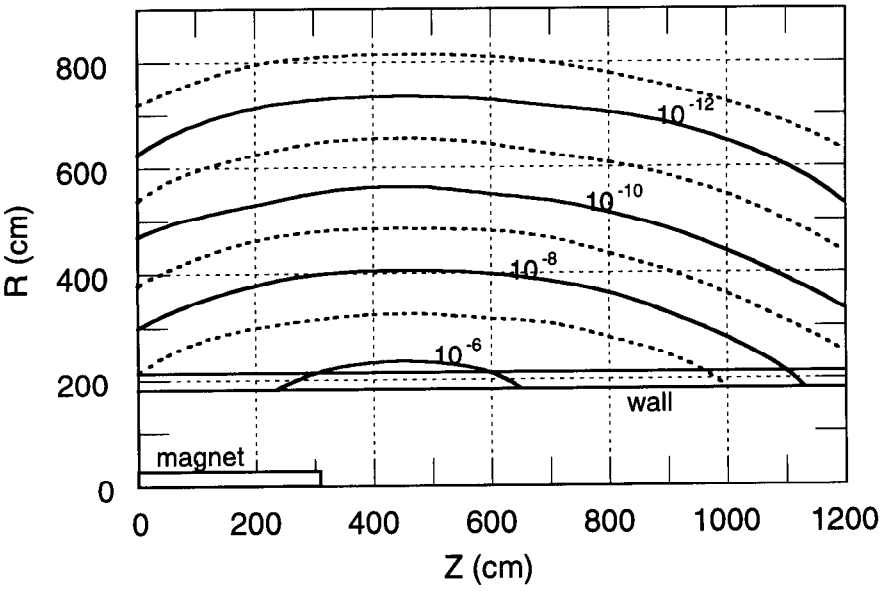

Fig. 3.15a Contour plots of equal star density calculated using CASIM for a 1 TeV proton beam incident "head on" on the inner edge of one of the pole pieces on standard deviation of beam width deep. The magnet was rectangular with an aperture was 3.8 x 12.7 cm and outer dimensions of 31.8 x 40.6 cm. The results were averaged over azimuth and the magnet was located in a tunnel 182 cm in radius. The concrete wall was 30.48 cm thick and was surrounded by soil. [Adapted from Co82b.]

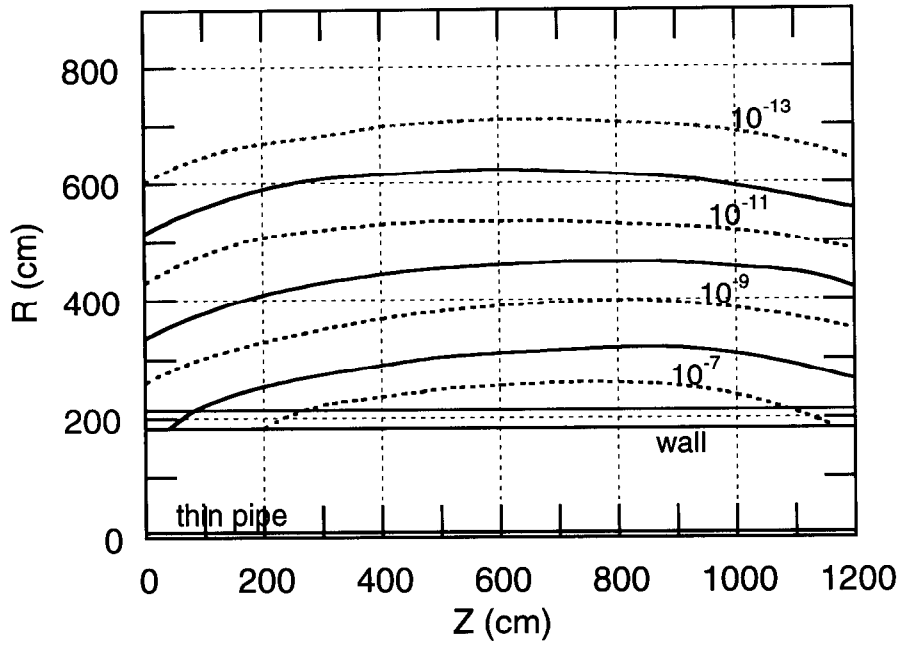

Fig. 3.15b Contour plots of equal star density calculated using CASIM for a 1 TeV proton beam incident "head on" on a thin aluminum pipe of 10.16 cm outside diameter with 0.318 cm thick walls. The results were averaged over azimuth and the pipe was located in a tunnel 182 cm in radius. The concrete wall was 30.48 cm thick and was surrounded by soil. [Adapted from Co82b.]

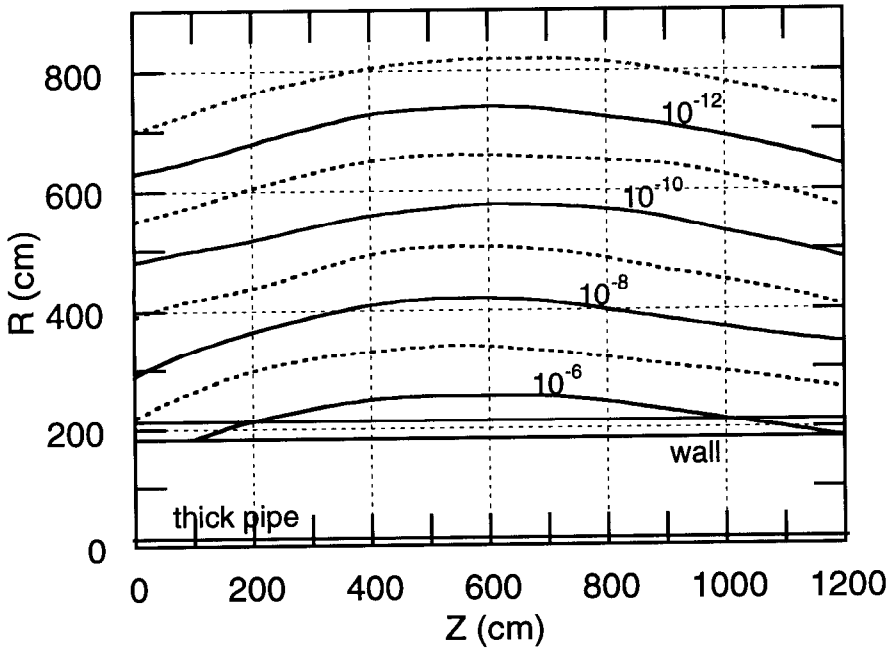

Fig. 3.15c Contour plots of equal star density calculated using CASIM for a 1 TeV proton beam incident "head on" on a thick iron pipe of 30.48 cm outside diameter with1.27 cm thick walls. The results were averaged over azimuth and the pipe was located in a tunnel 182 cm in radius. The concrete wall was 30.48 cm thick and was surrounded by soil. [Adapted from Co82b.]

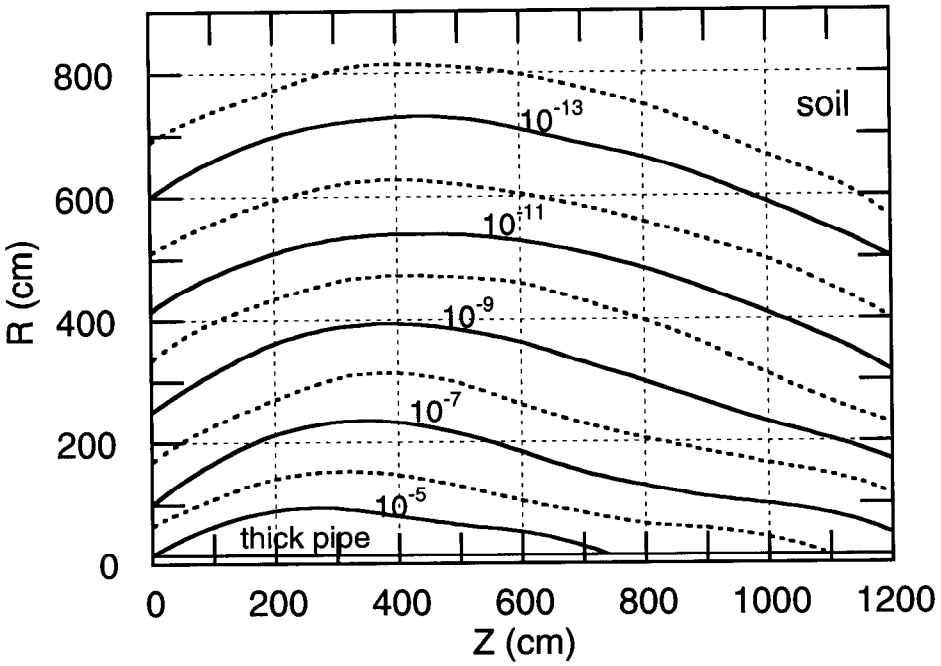

Fig. 3.15d Contour plots of equal star density calculated using CASIM for a 1 TeV proton beam incident "head on" on a thick iron pipe of 30.48 cm outside diameter with1.27 cm thick walls. The pipe is surrounded by soil of density $\rho = 2.25$ g cm^2. [Adapted from Co82b.]

Shielding Against Muons at Proton Accelerators

Muon production has been discussed previously in Chapter 1. At the higher energies, there are significant complications in that muon creation mechanisms in addition to pion and kaon production and subsequent decay are possible. However, the muons from pion and kaon decay generally, but not universally, represent the most important consideration in practical shielding calculations. In Monte-Carlo calculations, it is straightforward to "create" muons and follow them through the shielding medium.

Muon transport is well understood. Because of the lack of strong interactions, their absorption cross sections in shielding materials are negligible. The energy loss is typically dominated by ionization and excitation of atomic electrons. Coulomb scattering alters their paths. Because of their higher masses, radiative energy losses do not become important until their energies reach approximately 100 GeV. Other energy loss mechanisms also become important at the higher energies. The range-energy relations for muons were discussed in Chapter 1.

The effect of beam loss mechanisms on dose at proton and ion accelerators is, however, considerably different than in the electron situation. The particle energy downgrades quickly in hadronic showers so the most penetrating muons must originate in the first few generations of the process. These energetic muons are not "smeared out" in a large volume of phase space as are the neutrons. However, geometric effects or deflections by magnetic fields encountered near the point of production can affect the muon fluence at large distances. Thus, the presence of large "empty" spaces, that is decay paths (vacuum or air), near the point of interaction provide opportunity for the pions or kaons to decay into muons before they can be removed by nuclear interactions in solid materials. This is particularly important for the typical situation of a target used to produce secondary beams followed (downstream) by an air or vacuum gap (the space for decay into muons) and then a beam dump. If magnetic fields are present, the muon fluence generally peaks in the bend plane. Multiple Coulomb scattering from nuclei is an important effect in muon transport. An appropriate Gaussian approximation of such scattering for all charged particles carrying electronic charge z (z = 1 for muons) having mean width θ_0 in space projected onto the plane of the initial direction of the particle is as follows:

$$\theta_0 = \frac{14.1(\text{MeV}/c)z}{p\beta}\sqrt{\frac{L}{X_0}}\left[1+\frac{1}{9}\left(\frac{L}{X_0}\right)\right] \text{ (radians)}, \tag{3.30}$$

where X_0 is the radiation length, p is momentum in MeV/c and L is the shield thickness in the same units as the radiation length. The distribution is described by the following function:

$$f(\theta)d\theta = \left(\frac{d\theta}{\theta_0\sqrt{2\pi}}\right)\exp\left(-\frac{\theta^2}{2\theta_0^2}\right). \tag{3.31}$$

Generally the most copious source of muons are those due to the decay of pions and kaons. There are several important facts about such muons that are summarized below.

A. The decay lengths (mean length for π or K to decay), Λ, are:

$\Lambda_\pi = 55.9p$ (meters), where p is the pion momentum in GeV/c,

$\Lambda_K = 7.51p$ (meters), where p is the kaon momentum in GeV/c.

The decay length can be used to estimate the total number of muons present. For example, a beam of 10^7 pions at 20 GeV/c will decay in a distance of 50 meters into 10^7 x [50 meters]/[56 x 20 meters decay length] = 4.5 x 10^5 muons. This uses the fact that the path length (50 meters) is small compared with the mean decay length of 1120 meters. If the path length, x, was comparable to the decay length, Λ, the intensity of 10^7 would be multiplied by the exponential factor $\{1 - \exp(x/\Lambda)\}$.

B. If $\beta \approx 1$, relativistic kinematics determines that the ratio, k_i, of the *minimum* momentum of the daughter muon ($p_{\min}$) to the momentum of the parent pion or kaon (p_i) is given by:

$$k_i = p_{\min}/p_{\text{parent}} = (m_\mu/m_{parent})^2 . \tag{3.32}$$

The result is that k_i has a value of 0.57 for muons with pion parents and 0.046 for muons with kaon parents. Thus if, say, a beam transport system restricts the momentum of pions to some minimum value, then a minimum value given by the above is placed on the muon momentum at the time of decay.

C. Since in the center of mass frame of reference the decay is isotropic, and there is a one-to-one relationship between the muon momentum and the angle of emission, for muon momenta >> m_{parent} (in units where $c = 1$) the momentum spectrum of the muons can be expressed as

$$\frac{dN}{dp} = \frac{1}{p_{parent}(1-k_i)} \tag{3.33}$$

This means that the spectrum of daughter muons uniformly extends from the momentum of the parent down to the minimum established in Eq. (3.32).

D. Relativistic kinematics also gives the result that the maximum angle, in the laboratory frame of reference, between the momentum vector of the muon and that of the parent particle is given by:

$$\tan\theta_{\max} = \frac{(m_{parent}^2 - m_\mu^2)}{2p_{parent}m_\mu} . \tag{3.34}$$

For muons originating from pion decay, θ_{max} is at most several milliradians. However, for muons originating from the decay of 5 GeV kaons, θ_{max} is a relatively large 12°. Thus $\pi -> \mu$ decays can be assumed to be collinear while $K -> \mu$ decays have significant divergence at the lower energies.

Monte-Carlo calculations are needed to adequately describe the production and transport of muons because of the sensitivity to details of the geometry which determine the pion and kaon flight paths and influence the muon populations. Schopper et al, (Sc90) has presented some useful information about the production of muons that one can use to make approximate estimates by giving calculated values of angular distributions of muon spectra with an absolute normalization from pion and kaon decays for one meter decay paths. Neither the effects of absorbers nor magnetic fields are included in these results. For other decay paths that are short compared with the decay length, one can simply scale by the length of the actual decay path. The results are displayed in Fig. 3.16.

Decays of other particles can be important sources of muons at higher energies, especially those found in hadron-hadron collisions at high energy colliders. Especially notable are those from charm (D) and bottom (B) meson decays (Sc90). The muons from these sources are often called "direct" muons due to the short lifetimes and decay lengths involved. The masses of these parent particles and their meanlives, τ, are as follows:

$$m(\mathrm{D}^{\pm}) = 1869.3 \pm 0.5 \text{ MeV}, \quad \tau = (10.66 \pm 0.23) \times 10^{-13} \text{ s}, \; c\tau = 320 \text{ μm}$$
$$m(\mathrm{B}^{\pm}) = 5278.6 \pm 2.0 \text{ MeV}, \quad \tau = (12.9 \pm 0.5) \times 10^{-13} \text{ s}, \; c\tau = 387 \text{ μm}.$$

Figures 3.17 and 3.18 give results for muons originating from these decays

An approximate method for calculating muon flux densities at proton accelerators has been developed by Sullivan (Su92) based upon a semi-empirical fit to existing muon production data. Sullivan gives an equation for the flux density of muons per meter of decay path as a function of shield thickness found along the proton beam axis (that is, on the straight-ahead maximum of the muons):

$$\phi = 0.085 \frac{Ex}{X^2} \exp\left\{-\frac{\alpha t}{E}\right\}, \tag{3.35}$$

where ϕ is the flux density (muons/m^2) per interacting proton, E is the proton beam energy (GeV), X is the distance of the point of concern to the point of production of the pions and kaons (meters), x is the average path length (i.e., the decay path) of the pions and kaons in air, gases, or vacuum prior to their absorption by solids or liquids, and α is an effective average energy loss rate (GeV/meter) for the muons in a shield of thickness t (meters). x can be taken to be the actual physical length of the decay path or, for a beam dump situation, according to Sullivan, can reasonably be taken to be 1.8 times the hadron nuclear interaction mean free path for the material comprising the beam dump. Values of α for typical shielding materials are:

α_{concrete} = 9.0 GeV/meter (for $\rho = 2.35$ g cm^{-3}),
α_{water} = 4.0 GeV/meter (for $\rho = 1.0$ g cm^{-3}),
α_{iron} = 23.0 GeV/meter (for $\rho = 7.4$ g cm^{-3}), and
α_{lead} = 29.0 GeV/meter (for $\rho = 11.3$ g cm^{-3}).

The value for concrete can be used for earth if one adjusts it to the correct density. It is obvious that the argument of the exponential in Eq. (3.35) can be expanded as the sum over the materials comprising a composite shield. Sullivan has also given a prescription for calculating the full width at half maximum (FWHM) of the muon distribution at the boundary of such a shield. This is given by:

$$FWHM = 4.6\frac{X}{\sqrt{\alpha E t}} \text{ (meters)}. \tag{3.36}$$

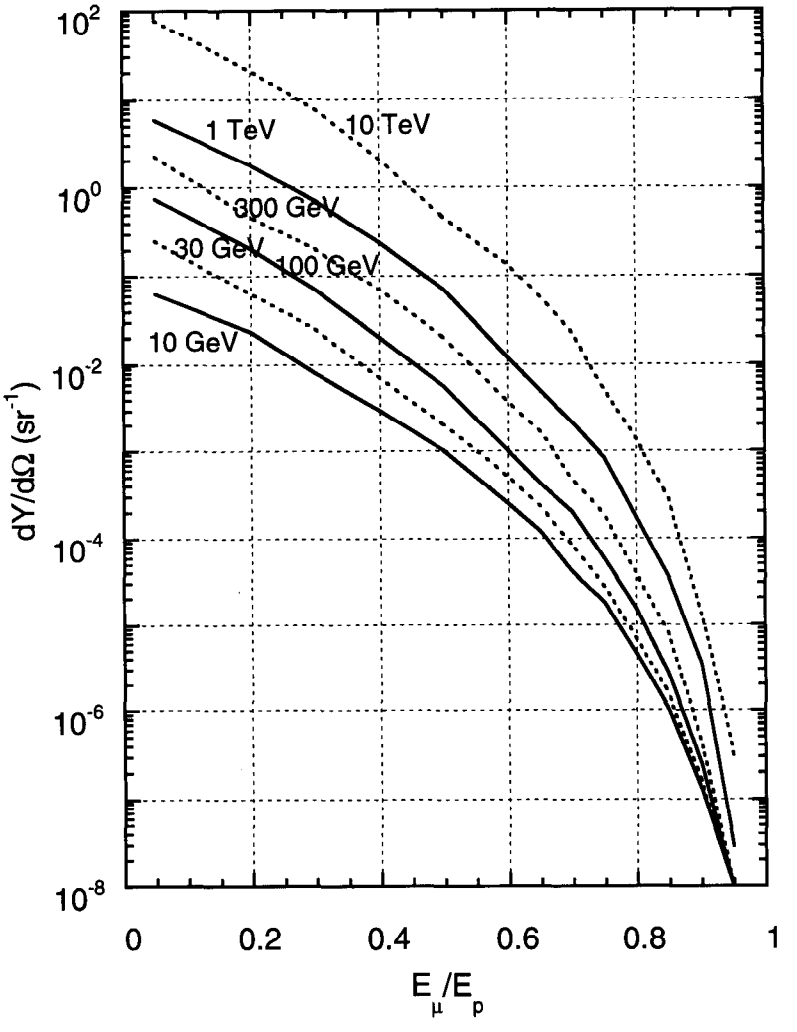

Fig. 3.16 Yield of muons from the decay of pions and kaons of both charges produced in proton-Fe collisions at several energies of the incident proton. The distance available for decay is assumed to be 1 meter. The abscissa, E_μ/E_p is the muon energy expressed as a fraction of the incident proton energy. The ordinate, $dY/d\Omega$, is the number of muons having an energy greater than E_μ, per incident proton sr^{-1}. All values are for $\theta = 0$. [Adapted from (Sc90).]

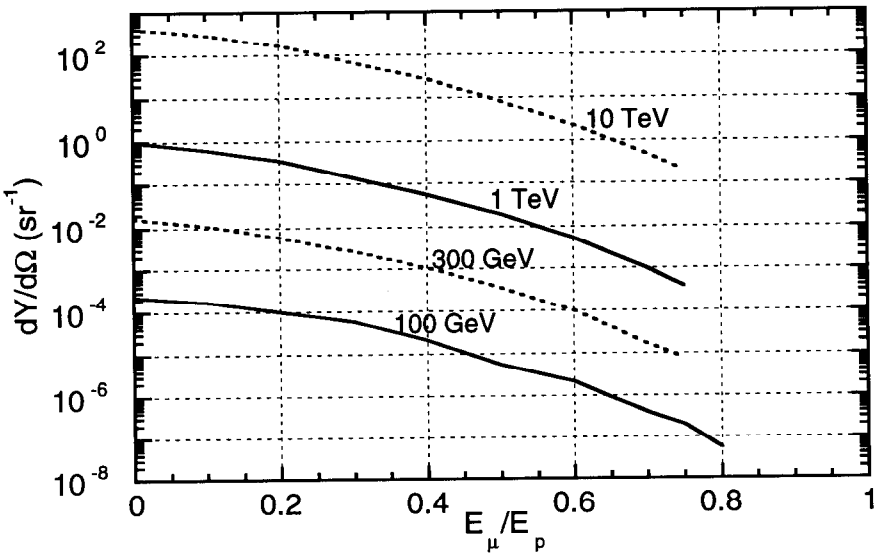

Fig. 3.17 Muons from the decay of D-mesons produced in proton-proton collisions at four incident proton energies and at $\theta = 0$. The abscissa, E_μ/E_p is the muon energy expressed as a fraction of the incident proton energy. The ordinate, $dY/d\Omega$, is the number of muons per unit solid angle per incident proton having an energy greater than E_μ, expressed in sr^{-1}. [Adapted from (Sc90).]

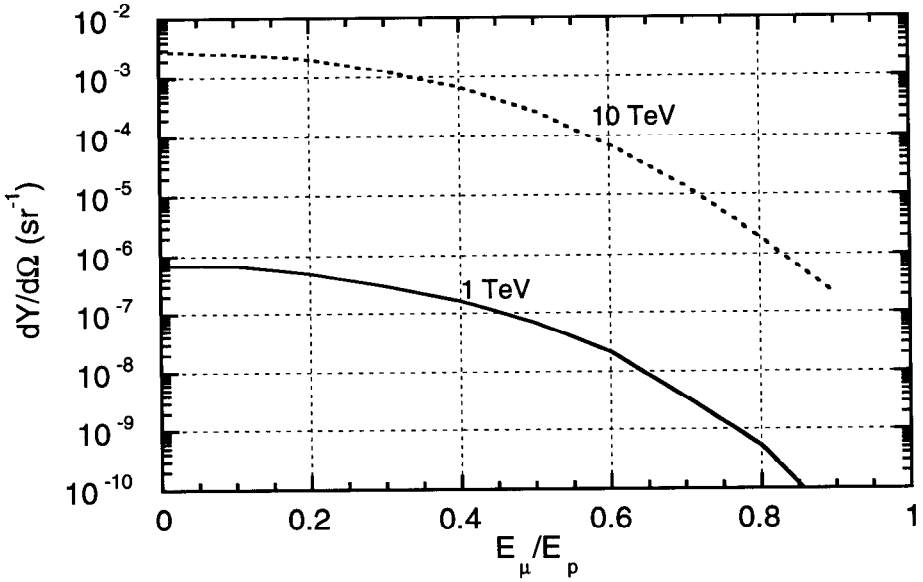

Fig. 3.18 Muons from the decay of B-mesons produced in proton-proton collisions at various energies of the incident proton and at $\theta = 0$. The abscissa, E_μ/E_p is the muon energy expressed as a fraction of the incident proton energy. The ordinate, $dY/d\Omega$, is the number of muons per unit solid angle per incident proton having an energy greater than E_μ, expressed in sr^{-1}. [Adapted from (Sc90).]

IV. Shielding Materials and Neutron Energy Spectra

Shielding Materials

Given the size of many modern accelerators, economic considerations often dominate shielding designs by requiring the use of relatively inexpensive, but less efficient shields. In all cases, good engineering practices concerning structural properties, appropriate floor loading allowances, and fire protection considerations must be appropriately taken into account to provide an acceptable degree of conventional safety. In general, low atomic number materials are best used for targets, collimators, and beam stops at electron accelerators to reduce photon production, while high atomic number materials are preferred at proton and heavy ion accelerators for these components to reduce neutron production. However, at ion energies above 5 MeV neutrons are produced in most materials. Some materials have superior heat transfer characteristics which enhances reliability and thus can reduce personnel exposures incurred in maintenance activities.

earth

Earth has many admirable qualities as a shield material besides its economy. The water it contains enhances the effectiveness of the neutron attenuation, yet it is composed of sufficiently high atomic number elements to be effective against photons. Representative ranges of soil water content (per cent of dry weight) are: sand (0-10), sandy loam (5-20), loam (8-25), silty loam (10-30), dry loam (14-30), and clay (15-30). Dry earth has a typical elemental composition as given in Table 3.6. Earth is generally a "crackless" shield, not prone to neutron leakage by "streaming". The density of earth varies widely, from as low as 1.7 $g \cdot cm^{-3}$ to as much as 2.25 $g \cdot cm^{-3}$, depending upon soil type and water content. Given this variation, specific knowledge of soil characteristics at the accelerator site are needed to do effective shielding designs. Definitive measurements of the water content are also most useful if the shielding of neutrons is the intent and no safety factors are being used.

concrete

Concrete has obvious advantages in that it can either be poured in place permanently or be cast into modular blocks. Sometimes concrete is used to shield targets, beam stops, etc. in a manner that allows their ready access if the need for maintenance arises. The use of concrete blocks generally requires the overlapping of the blocks to avoid streaming through the cracks. It is sometimes efficient to use a heavy material as part of the aggregate in the concrete recipe. This can increase the density of the material as well as its average atomic number. The latter, of course, increases the effectiveness against photons. Table 3.7 gives some partial densities of various concretes used in shielding. When shielding neutrons, the water content is quite important because it incorporates almost all of the hydrogen. Under extreme low-humidity conditions, the water content of concrete can decrease with time, to as little as 50 % of the initial value over a 20 year period. The density of concrete is locally variable.

other hydrogenous materials

Polyethylene and other materials subject to boration: Polyethylene, $(CH_2)_n$, is a very effective neutron shield because of its hydrogen content (14% by weight) and its density (0.92 $g \cdot cm^{-3}$). The addition of boron can reduce the buildup of 2.2 MeV photons released in the thermal neutron capture by hydrogen by instead capturing the thermal neutrons in the boron, where the decay reaction produces an easily attenuated α-particle plus a more readily attenuated 0.48 MeV photon. Commercially, polyethylene is available including additives of boron (up to 32%), lithium (up to 10 %) and lead (up to 80 %) in various forms such as planer sheets, spheres, and cylinders. These materials can be useful, if it is necessary, to economize on space and also to accomplish shielding of photons and neutrons simultaneously. Pure polyethelyene is flammable, but some of the commercial products available contain self-extinguishing additives. Some of these materials are available in powder form, for molding into a desired shape by the user. Besides polyethylene, boron has been added to other materials to form effective thermal neutron shields. These include other plastics, putties, clays, and glasses to accomplish specific shielding objectives.

The three materials water, wood, and paraffin are superficially attractive neutron shields because of their very high hydrogen contents.

Water, of course, tends to rust out its containers and there is the omnipresent question as to whether the shield material has flowed away. Exposed to thermal neutrons, it also emits the 2.2 MeV capture γ-ray from hydrogen. The addition of boron is more difficult because of the relative insoluability of boron salts in water.

Wood was found in the early years of operation at the Bevatron at Berkeley to be as effective as concrete for shielding intermediate energy neutrons per unit length. Thus it is essential that the neutron energy spectrum to be attenuated is known. In the past wood has been discouraged as a shielding material because of its flammability. Recently, chemically treated wood that is nearly completely fireproof has become available, but it is not clear that the flammability problem has been solved with complete satisfaction. For example, questions have been raised by reports of a reduction in structural strength of such treated wood products.

Paraffin historically has been used for neutron shielding but has been spurned in recent years because of the fire hazard. Under some conditions it can be used if it is packaged in metal containers. Recently, paraffin treated with fire retardant additives has become available. It is still subject to "plastic" flow problems.

iron

A relatively high density, in conjunction with its low cost, make iron an attractive shielding material. Caution is required because the density can vary widely from a low of 7.0 for low grade cast iron to a high value of 7.8 $g \cdot cm^{-3}$ for some steels. The "textbook" value of 7.87 $g \cdot cm^{-3}$ given in Table 1.2 is almost never attained in the bulk quantities necessary for radiation shielding. Because of its nonmagnetic properties and resistance to corrosion, stainless steel is often used as part of accelerator components. Because of concerns about radioactivation, a knowledge of the elemental composition of various alloys can sometimes be of interest. For example, long-lived ^{60}Co can be produced in stainless steel but not in pure iron. Iron has a very important deficiency as a neutron shield; this will be discussed later in this chapter.

high atomic number materials

The materials in this category are valuable because of their high atomic number, especially where the shielding of photons is important. The most obvious material in this category is lead. It has high density (11.3 $g \cdot cm^{-3}$) and is resistent to corrosion. Pure lead, as is well known, has major drawbacks because of its poor structural characteristics and low melting point (327.4 ^{o}C). It is usually best used when it can be laminated to some other, more structurally stable, material. Some alloys represent improvements on the structural properties. It is often available as an additive to other materials in order to improve their capacity for shielding photons. Fabric blankets containing shredded lead can be effectively used to shield radioactivated components to minimize exposures associated with accelerator maintenance activities. The high chemical toxicity of lead requires care in its fabrication and handling to properly protect personnel.

Tungsten is an excellent, but relatively expensive, shielding material. Its high density (19.3 $g \cdot cm^{-3}$) and high melting temperature (3410 ^{o}C) make it extremely useful as a component in photon shields and in beam collimators.

Uranium is a somewhat attractive shielding material, most often in its "depleted" form in which ^{235}U is removed from the naturally dominant ^{238}U down to some residual fraction (usually 0.2 %) much lower than the natural value of 0.72 %. Its high density (19.0 $g \cdot cm^{-3}$) and relatively high melting point (1133 ^{o}C) are positive attributes, especially in places where space efficiency is a concern. It is obviously not a good choice of material in environments having a high neutron flux density due to its susceptability to fission induced by fast neutrons. In the depleted form, it is relatively safe, but if combined with hydrogenous materials, nuclear fission criticality should be considered for the specific material and geometric arrangement to be employed. Even in the absence of hydrogen, thermal neutrons under certain conditions can result in the possibility of criticality. Major drawbacks are its material properties. It has a large anisotropic thermal expansion coefficient and also readily oxidizes when exposed to air (especially humid air). The oxide is readily removable and presents a significant internal exposure hazard.

Prevention of oxidation by sealing it with epoxy or paint meets with only limited success due eventual embrittlement and chipping accelerated by radiation damage. Sealed containers filled with dry air or with noble gases or liquified noble gases such as argon seem to represent the best storage solution to limit oxide formation. Small chips of this element are also pyrophoric, complicating machining-type processes by posing yet another safety hazard.

beryllium, aluminum, and zirconium

These three materials find considerable usage as accelerator components because of various properties. Beryllium is often used as a target material in intense beams because of its resistance to thermal effects (especially when in the form of the oxide, BeO). It has been used at high energy accelerators in relatively large quantites as a "filter" to enrich one particle type at the expense of another. A serious concern is the extreme chemical toxicity of the metal and its compounds, which makes it difficult to fabricate. Aluminum is used as an accelerator component because of its nonmagnetic properties and its resistence to corrosion. It is not an effective shield against neutrons. Zirconium has a very small thermal neutron capture cross section and very good thermal properties. It is therefore not a good neutron absorber but has been found to be useful in beam-handling component material in some situations.

Table 3.6 Elemental composition, dry-weight percent basis, of representative soils. [Adapted from (Ch84).]

Element	Global Average (%)
O	43.77
Si	28.1
Al	8.24
Fe	5.09
Mn	0.07 ± 0.06
Ti	0.45 ± 0.43
Ca	3.65
Mg	2.11
K	2.64
Na	2.84

Table 3.7 Partial densities of representative concretes after curing. [Adapted from (Ch84).]

Type: Additive	Ordinary	Magnetite (FeO, Fe_2O_3)	Barytes $BaSO_4$	Magnetite & Fe
Density (g/cm^3)	2.34	3.53	3.35	4.64
H	0.013	0.011	0.012	0.011
O	1.165	1.168	1.043	0.638
Si	0.737	0.091	0.035	0.073
Ca	0.194	0.251	0.168	0.258
Na	0.040			
Mg	0.006	0.033	0.004	0.017
Al	0.107	0.083	0.014	0.048
S	0.003	0.005	0.361	
K	0.045		0.159	
Fe	0.029	1.676		3.512
Ti		0.192		0.074
Cr		0.006		
Mn		0.007		
V		0.011		0.003
Ba			1.551	

Measured Neutron Energy Spectra Outside of Shields

In the most simple approximation, outside of thick shields of soil or concrete that contain some hydrogen content (usually in the form of H_2O), accelerator neutron shields can most generally said to be a "1/E" spectrum with the energies extending from those of thermal neutrons ($\langle E_n \rangle$ = 0.025 eV) up to the energy of the incident protons. In this approximation, the spectrum is given as:

$$\frac{d\phi(E)}{dE} = k\frac{1}{E}, \tag{3.37}$$

where k is a normalizing constant. Rohrig (Ro83) observed from this that it is more convenient to plot such spectra as flux per *logarithmic* energy interval by simply plotting $E\phi(E)$;

$$\frac{d\phi(E)}{d\ln E} = E\phi(E)\ . \tag{3.38}$$

In the terminology of textbooks on "neutron physics", this is also called a "lethargy" plot. It, effectively, suppresses the 1/E dependence seen in typical neutron energy spectra.

Detailed features of the geometry involved can produce peaks in the neutron energy spectrum. Some of these have been discussed by various workers (Pa73, Nc96, Th88, El86, and Co88). These peaks are typically encountered in the few MeV region. Figures 3.19, 3.20, 3.21 and 3.22 are plots of neutron spectra and sketches

of the shielding geometry involved taken from Cossairt et al. (Co88). These spectra were obtained (i.e., "unfolded") using the Bonner sphere technique discussed in more detail in Chapter 6. In these figures, "spheres" denote the locations where the neutron energy spectra were measured. These are typical of the spectra found at high energy proton accelerators. Figure 3.19 is rather typical of the spectra found external to earth and concrete shields lateral to high energy proton accelerators. The neutron energy spectrum displayed in Fig. 3.20 is particular interesting because its shape was demonstrated to be essentially independent of proton energy over the range of 150 to 900 GeV (McC88).

One of the peaks which commonly appear in such spectra is particularly important. As discovered by Alsmiller and Barish (Al73), iron has a major deficiency as a shield for fast neutrons. Containing no hydrogen, the primary attenuation mechanism for fast neutrons is by inelastic scattering from the iron nuclei. At energies below the first excited state of any nucleus, inelastic scattering becomes impossible and elastic scattering becomes the only removal process. Elastic scattering is a very inefficient mechanism for energy removal for neutrons scattering off the much more massive iron nucleus. The scattering of billiard balls off of bowling balls comes to mind as an analogy. It is intuitive that billiard balls scattering off other billiard balls of equal mass provides for much more efficient energy transfer. Likewise, neutrons scattered by the "free" protons in hydrogenous materials is much more efficient in terms of energy transfer than is the elastic scattering of neutrons from iron nuclei. The first excited state of ^{56}Fe, which is the dominant (92%) isotope in natural iron, is at 847 keV. This has the consequence that the neutrons build up below this energy due to the inefficiency of the transfer of energy by means of elastic scattering. Thus neutrons above 847 keV in a given spectrum will be slowed by inelastic scattering only to build up in this region. Amplifying this effect when one considers the dose equivalent external to such shields is the fact that the quality factor for neutrons as a function of energy also has its maximum value at about 700 keV. Thus, pure iron shields are rather ineffective in attenuating neutrons in this energy region. This phenonmena is illustrated by the spectra shown in Fig. 3.21. Both spectra shown were measured at about $\theta = 90^{o}$ from a beam dump struck by secondary particles due to 800 GeV proton interactions far upstream of the beam dump (El86). The beam dump was shielded by the yoke of a large iron magnet schematically shown in Fig. 3.21a. Originally, the neutron energy spectra was measured directly adjacent to this iron shield. This spectra is identified as Fig. 3.21b. Later, in order to reduce the intensity of the neutron radiation, concrete shielding blocks 91.4 cm thick were placed between the neutron detectors and the beam absorber. The neutron energy spectra was measured again with the result displayed in Fig. 3.21c. For the bare iron situation the dose equivalent rate external to the shield was over 40 times that measured after the concrete was installed. This factor is far in excess of the approximate factor of 10 expected from simple attenuation of the equilibrium cascade neutron spectrum. The concrete also reduced the average quality factor from 5.4 to 2.8. In general, an iron shield "capped" or "backed" by such a concrete shield will be an efficient use of space. It has been determined that 60 cm of concrete is the most efficient thickness to use for this purpose

[(Yu83) and (Za87)]. Shielding properties of other elements near iron (chiefly copper and nickel) in the periodic table are comparable. Fig. 3.22 is typical of the results obtained in the second section ("leg") of a labyrinth penetration.

One must be concerned with the relative amounts of fluence and dose equivalent due to specific spectral regions. This can affect the potential to produce radioactivity and also guides the designer of shielding. Tables 3.8 and 3.9 give these properties for the spectra displayed in Figs. 3.19-22. Fig. 3.23 is a plot of cumulative values of the same quantities for 1000 GeV protons incident on the face of a thick cylindrical concrete shield. As determined by Van Ginneken and Awschalom (Va75), the dependence upon incident proton energy of the distributions of fluence and dose equivalent is slight.

Table 3.8 Percent fluence in specific energy bins for neutron energy spectra. [Adapted from (Co88).]

Energy Range	Fig. 3.19	Fig. 3.20	Fig. 3.21b	Fig. 3.21c	Fig. 3.22
< 1.5 eV	31.5	19.5	28	55	71
0.0015 - 100 keV	12.5	36	46	43	24
0.1 - 2 MeV	8.5	36	17.5	2	2
2 - 25 MeV	40.5	7	4.5	0.1	1
> 25 MeV	7	1.5	4	0	1.5

Table 3.9 Percent of dose equivalent in specific energy bins for neutron energy spectra along with average quality factor. [Adapted from (Co88).]

Energy Range	Fig. 3.19	Fig. 3.20	Fig. 3.21b	Fig. 3.21c	Fig. 3.22
< 1.5 eV	1.5	2	4	41.5	32
0.0015 - 100 keV	0.5	6	11.5	37	16
0.1 - 2 MeV	9	58.5	35	17	9
2 - 25 MeV	75	26	24	3.5	13
> 25 MeV	14	7.5	25	1	30
Average Quality Factor	5.8	6.9	5.4	2.5	3.1

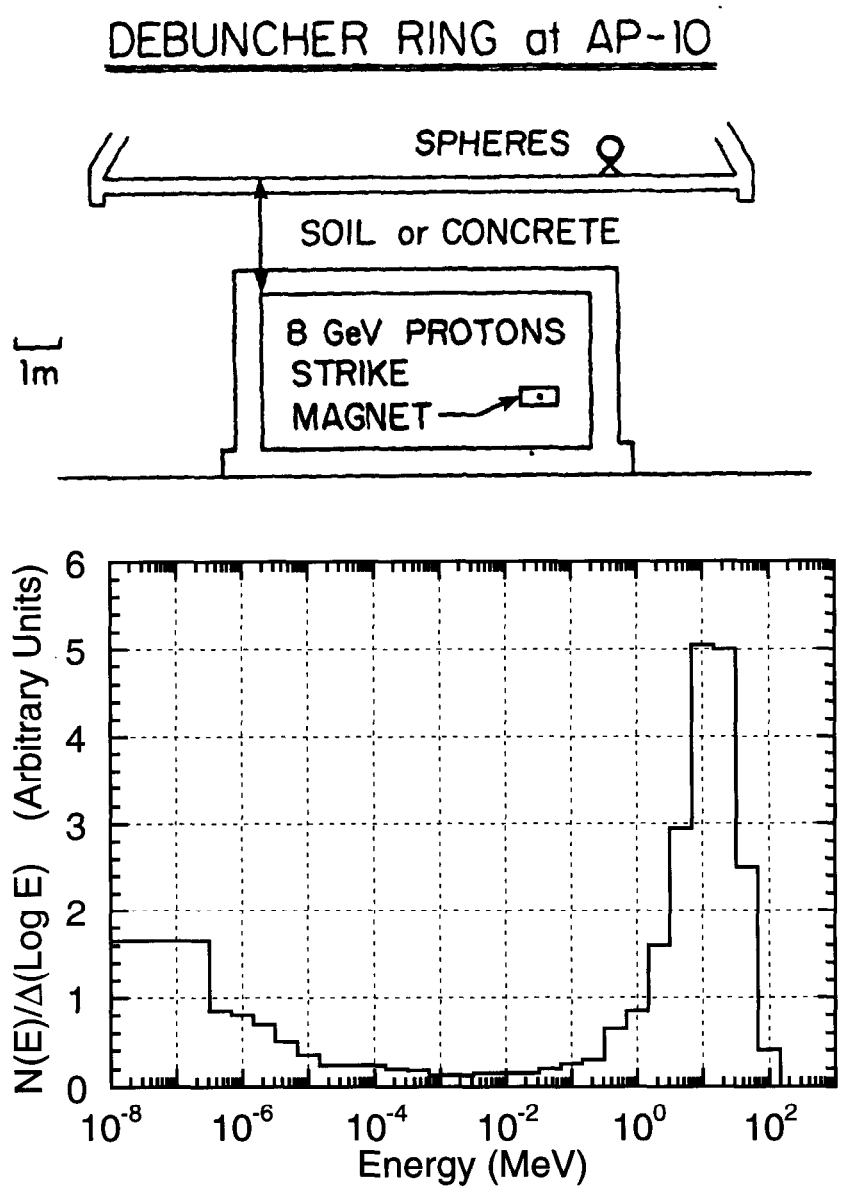

Fig. 3.19 Neutron energy spectra obtained external to a beam enclosure in which 8 GeV protons struck the yoke of a magnet. The site was the Fermilab Debuncher Ring. The normalization of the spectrum is arbitrary. [Adapted from (Co88).]

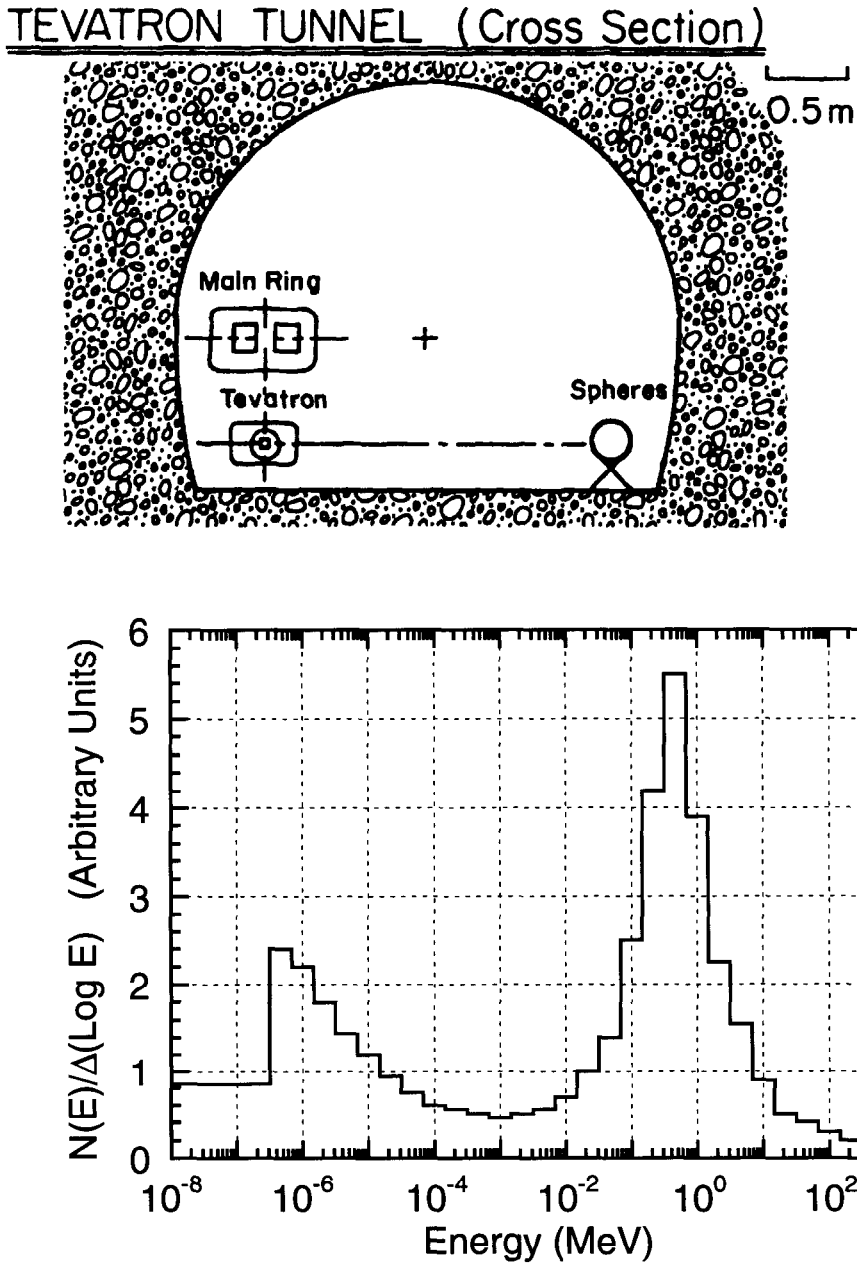

Fig. 3.20 Neutron energy spectra obtained internally in a beam enclosure in which 800 GeV protons interacted with residual gas in the Tevatron vacuum chamber during circulating beam conditions. The site was the Fermilab Tevatron Ring. The normalization of the spectrum is arbitrary. [Adapted from (McC88).]

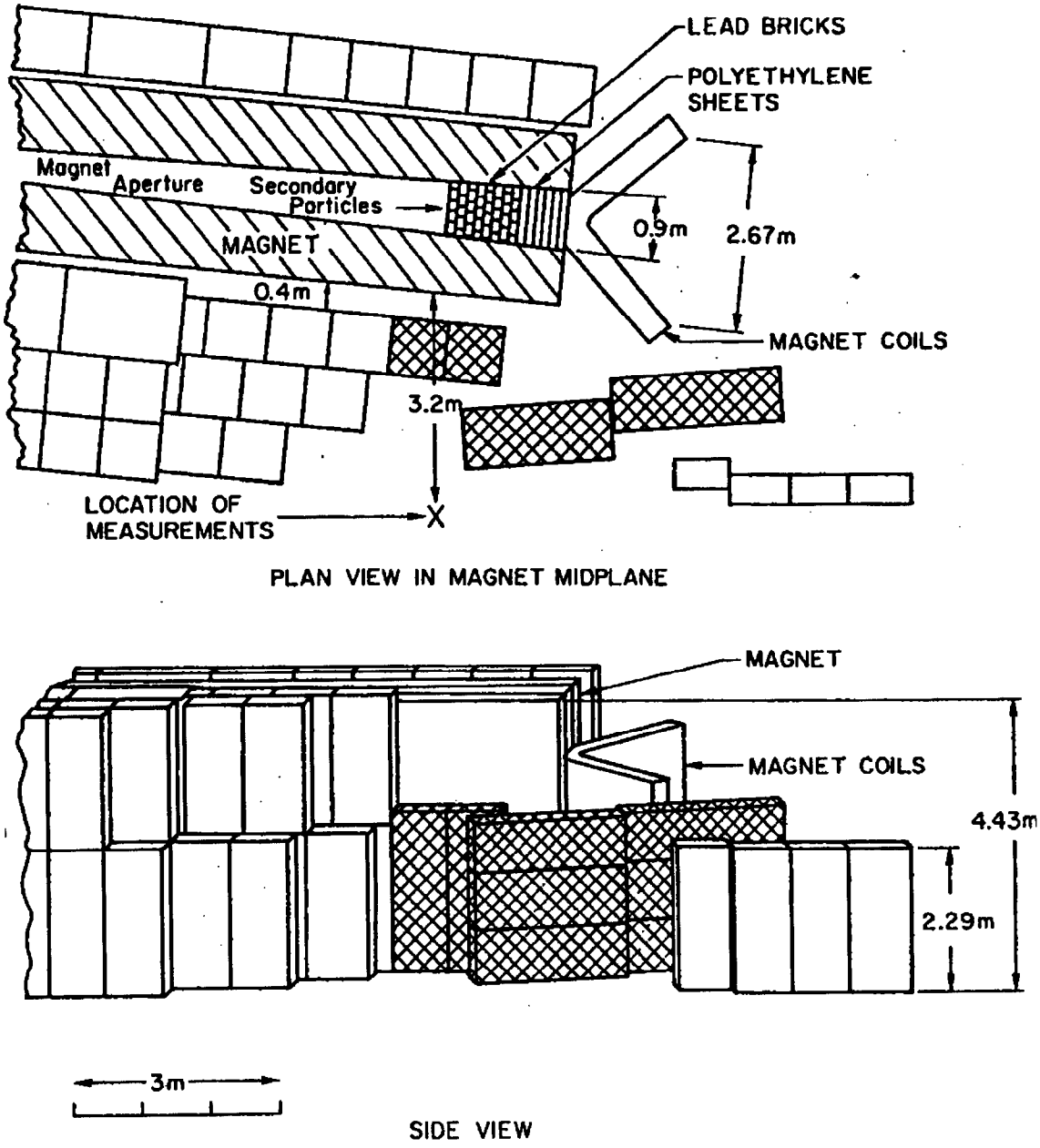

Fig. 3.21a Situation for the measurements shown in Figs. 3.21b and 3.21c. A target upstream (to the left) of the figure was struck by 800 GeV protons. Secondary particles produced by these interactions were intercepted by the beam absorber shown in the Figure. During initial operations, the cross-hatched blocks were not in place between this beam absorber and the location of measurements and the result was the measured spectrum in Fig. 3.21b. Later, those blocks were added and the spectrum shown in Fig. 3.21c was measured. [Reproduced from (El86).]

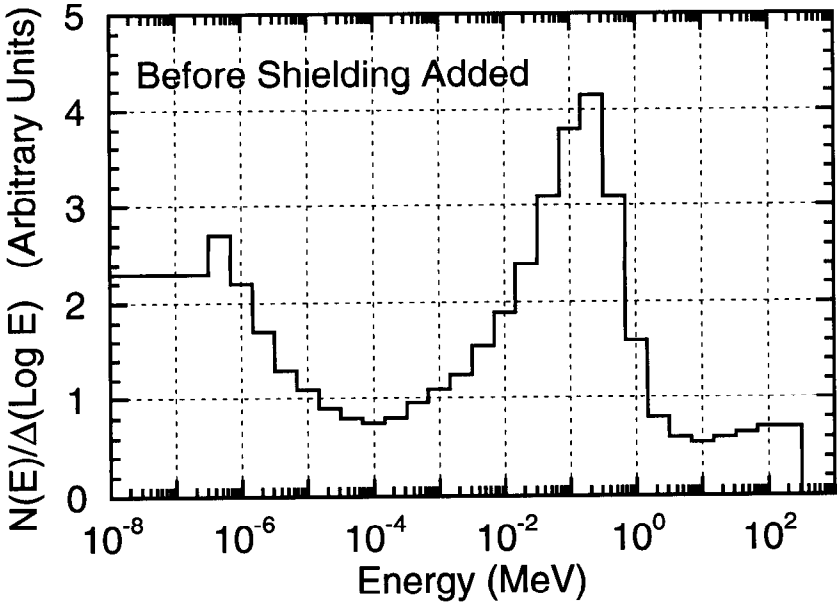

b)

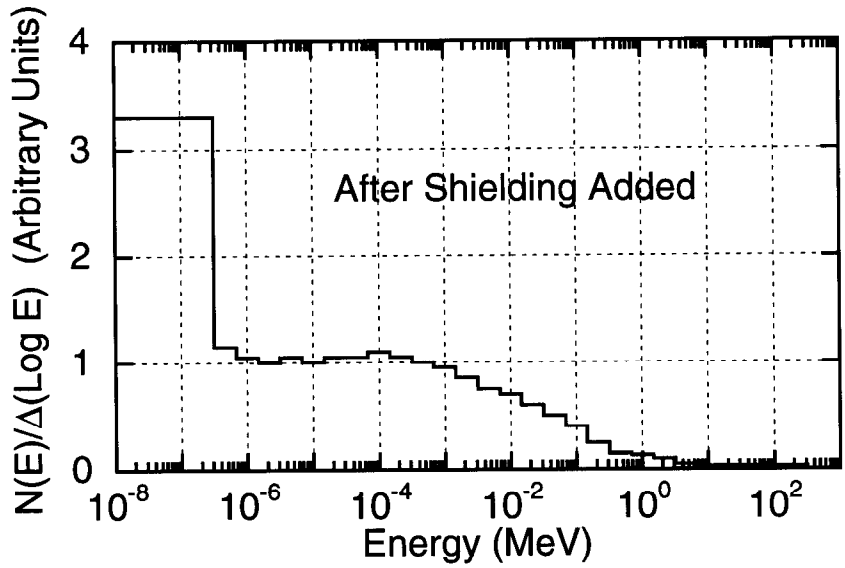

c)

Fig. 3.21 b&c Neutron energy spectra obtained external to the shielding configuration shown in Fig. 3.21a for the two different situations discussed above. The normalization of the spectrum is arbitrary. [Adapted from (El86).]

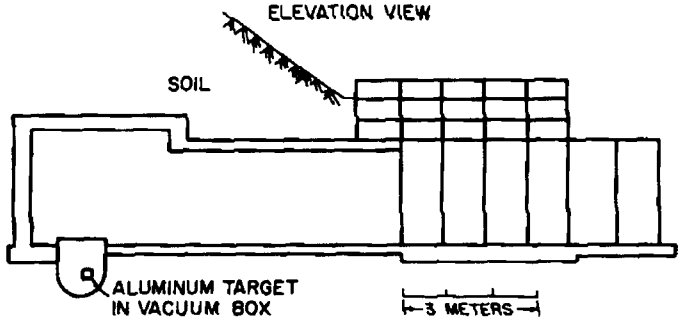

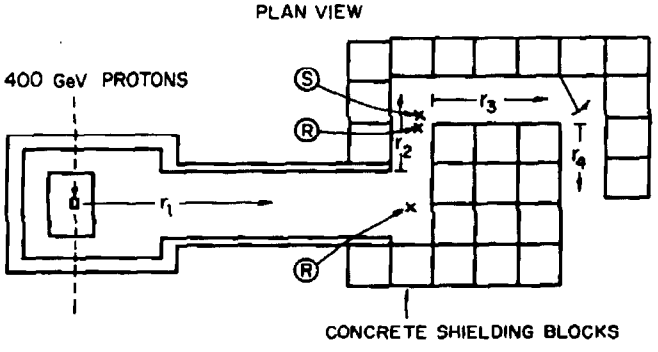

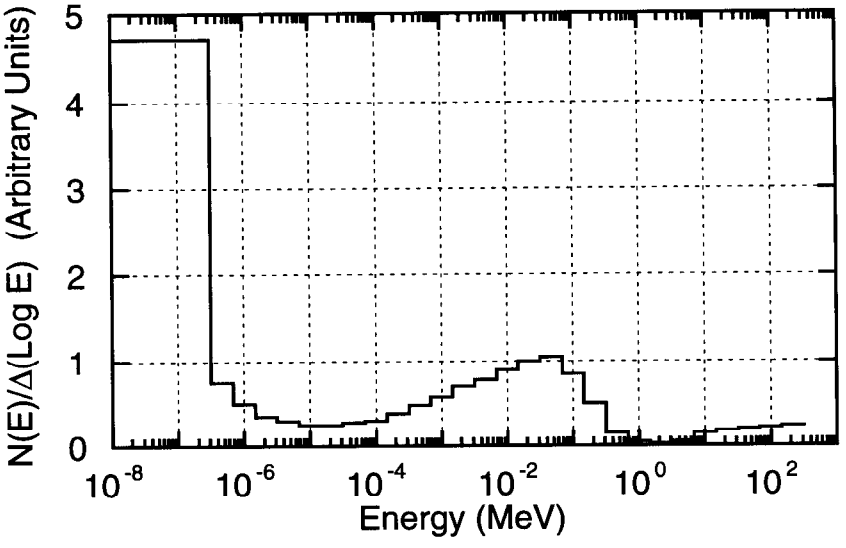

Fig. 3.22 Neutron energy spectra obtained within a labyrinth enclosure in which 400 GeV protons interacted with an aluminum target located beneath the floor of the enclosure shown. The spectrum was measured in the second leg at the location denoted "S". The normalization is arbitrary. [Adapted from (Co88).]

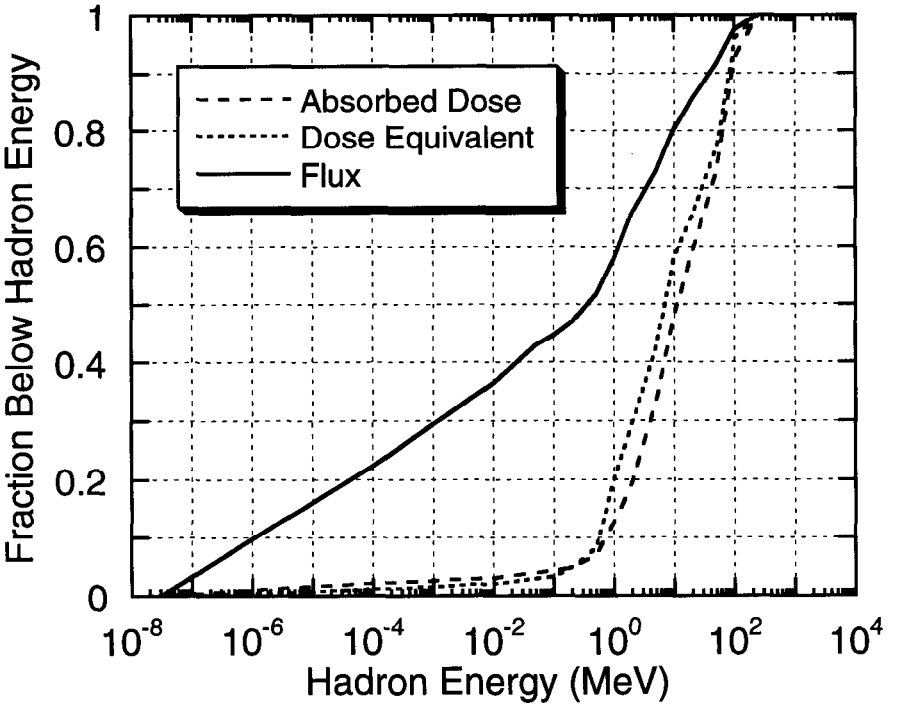

Fig. 3.23 Fraction of the omnidirectional flux, entrance absorbed dose, and maximum dose equivalent below hadron kinetic energy on abscissa (in MeV) for the region between zero and 450 cm depth and between 300 cm and 750 cm radius for 1000 GeV/c protons incident on the face of a solid concrete cylinder. [Adapted from (Va75).]

References

(Aa86) P. A. Aarnio, A. Fassò, H. J. Moehring, J. Ranft, G. R. Stevenson, "FLUKA86 users guide", CERN Divisional Report TIS-RP/168 (1986).

(Al73) R. G. Alsimiller, Jr, and J. Barish, "Shielding against the neutrons produced when 400 Mev elecrons are incident on a thick copper target", Particle Acceleraters 5 (1973) 155-159.

(Al75) R. G. Alsmiller, R. T. Santoro,, and J. Barish, "Shielding calculations for a 200 MeV proton accelerator and comparisons with experimental data", Particle Accelerators 7 (1975) 1-7.

(Ar80) T. W. Armstrong, "The HETC hadronic cascade code", in *Computer techniques in radiation transport and dosimetry,* W. R. Nelson and T. M. Jenkins, editors (Plenum Press, New York and London, 1980), pp. 373-375.

(Ch84) A. B. Chilton, J. K. Shultis, and R. E. Faw, *Principles of radiation shielding* (Prentice-Hall, Englewood Cliffs, New Jersey, 1984).

(Ci65) A. Citron, L. Hoffmann, C. Passow, W. R. Nelson, and M. Whitehead, "A study of the nuclear cascade in steel initiated by 19.2 GeV/c protons, Nucl. Instrum. Meth. 32 (1965) 48-52.

(Cl71) F. H. Clark, "Shielding Data" Appendix E, in *Protection against neutron radiation* , NCRP Report No. 39 (Washington, DC, 1971).

(Co82a) J. D. Cossairt, N. V. Mokhov, and C. T. Murphy, "Absorbed dose measurements external to thick shielding at a high energy proton accelerator: Comparison with Monte-Carlo calculations, Nucl. Instr. and Meth. 197 (1982) 465-472.

(Co82b) J. D. Cossairt, "A collection of CASIM calculations", Fermilab Report TM-1140 (1982).

(Co85) J. D. Cossairt, S. W. Butala, and M. A. Gerardi, "Absorbed dose measurements at an 800 GeV proton accelerator, comparison with Monte-Carlo calculations, Nucl. Instr. and Meth., A238 (1985) 504-508.

(Co88) J. D. Cossairt, A. J. Elwyn, W. S. Freeman, W. C. Salsbury, and P. M. Yurista, "Measurement of neutrons in enclosures and outside of shielding at the Tevatron", Fermilab-Conf-88/106 (1988) also in *Proceedings of the 22nd Midyear Meeting of the Health Physics; Topical Meeting on Instrumentation*, San Antonio, TX, December, 1988, pp. 190-199.

(Co89a) J. D. Cossairt, A. J. Elwyn, W. S. Freeman, and S. W. Butala, "A study of the transport of high energy muons through a soil shield at the Tevatron", Nucl. Instr. and Meth. A276 (1989) 78-85.

(Co89b) J. D. Cossairt, A. J. Elwyn, and W. S. Freeman, "A study of the production and transport of high energy muons through a soil shield at the Tevatron", Nucl. Instr. and Meth. A276 (1989) 86-93.

(Co97) J. D. Cossairt, N. L. Grossman, and E. T. Marshall, "Assessment of dose equivalent due to neutrinos", Health Phys. 73 (1997) 894-898.

(El86) A. J. Elwyn and J. D. Cossairt, "A study of neutron leakage through an Fe shield at an accelerator", Health Physics 51 (1986) 723-735.

(Fa93) A. Fassò, A. Ferrari, J. Ranft, P.R. Sala, "FLUKA: present status and future developments", Proc. IV Int. Conf. on Calorimetry in High Energy Physics, La Biodola, Italy, 21-26 Sept. 1993, Ed. A. Menzione and A. Scribano, World Scientific, p. 493.

(Ga85) T. A. Gabriel, "The high energy transport code HETC", Oak Ridge National Laboratory Report ORNL-TM-9727 (1985).

(IC78) International Commission on Radiation Units and Measurements, "Basic aspects of high-energy particle interactions and radiation dosimetry", ICRU Report No. 28, Washington, DC, 1978.

(Ka89) A.N. Kalinovskii, N.V. Mokhov, and Yu.P. Nikitin, "Passage of high-energy particles through matter", American Institute of Physics, NY (1989).

(Kr97) O.E. Krivosheev and N.V. Mokhov, "A new MARS and its applications", Fermilab-Conf-98/043 (1998) and SARE3 KEK Proceedings 97-5 (1997).

(Li61) S. J. Lindenbaum, "Shielding of high energy accelerators", Ann. Rev. Nucl. Sci. 11 (1961) 213-258.

(McC85) J. B. McCaslin, P. R. LaPlant, A. R. Smith, W. P. Swanson, and R. H. Thomas, "Neutron production by Ne and Si ions on a thick Cu target at 670 MeV/A with application to radiation protection," IEEE Trans. on Nucl. Sci. NS-32, No. 5 (1985) 3104.

(McC87) J. B. McCaslin, W. P. Swanson, and R. H. Thomas, "Moyer model approximations for point and extended beam losses", Nucl. Instr. and Meth. A256 (1987) 418-426.

(McC88) J. B. McCaslin, R.-K. Sun, W. P. Swanson, J. D. Cossairt, A. J. Elwyn, W. S. Freeman, H. Jöstlein, C. D. Moore, P. M. Yurista, and D. E. Groom, "Radiation environment in the tunnel of a high-energy proton accelerator at energies near 1 TeV," Lawrence Berkeley Report LBL-24640 (1987), presented at the Seventh Annual Congress of the International Radiation Protection Association, Sydney, Australia, April, 1988.

(Mo86) N. V. Mokhov and J. D. Cossairt, "A short review of Monte Carlo hadronic cascade calculations in the multi-TeV energy region", Nucl. Instr. and Meth. A244 (1986) 349-355.

(Mo95) N.V. Mokhov, "The MARS code system Users Guide, version 13(95)", Fermilab Report FN-628 (1995).

(Pa73) H. W. Patterson and R. H. Thomas, *Accelerator health physics,* (Academic Press, New York, 1973).

(Ro76) J. T. Routti and R. H. Thomas, "Moyer integrals for estimating shielding of high-energy accelerators", Nucl. Instr. and Meth. 76 (1969) 157-163.

(Ro83) N. Rohrig, "Plotting neutron fluence spectra, Health Physics 45 (1983) 817-818.

(Sc90) H. Schopper (editor), A. Fassò, K. Goebel, M. Höfert, J, Ranft, and G. Stevenson, *Landolt-Börnstein numerical data and functional relationships in science and technology New Series; Group I: Nuclear and particle physics Volume II: Shielding against high energy radiation* (O. Madelung, Editor in Chief, Springer-Verlag, Berlin, Heidelberg, 1990).

(St82) G. R. Stevenson, L. Kuei-Lin, and R. H. Thomas, "Determination of transverse shielding for proton accelerators using the Moyer model", Health Phys. 43 (1982) 13-29.

(St86) G. R. Stevenson, "Dose equivalent per star in hadron cascade calculations", CERN Divisional Report TIS-RP/173 (1986). [Also in Schopper et al. (Sc90)].

(St87) G. R. Stevenson, "Empirical parametrization of the shielding of end-stops at high-energy proton accelerators, CERN Divisional Report TIS-RP/183/CF (1987).

(Su92) A. H. Sullivan, *A guide to radiation and radioactivity levels near high energy particle accelerators* (Nuclear Technology Publishing, Ashford, Kent, United Kingdom), 1992)

(Te83) K. Tesch, "Comments on the transverse shielding of proton accelerators", Health Phys. 44 (1983) 79-82.

(Te85) K. Tesch, "A simple estimation of the lateral shielding for proton accelerators in the energy range from 50 to 1000 MeV," Rad. Prot. Dos. 11 (1985) 165-172.

(Th84) R. H. Thomas and S. V. Thomas, " Variation and regression analysis of Moyer model parameter data", Health Phys. 46 (1984) 954-957.

(Th88) R. H. Thomas and G. R. Stevenson, "Radiological safety aspects of the operation of proton accelerators", Technical Report No. 283, International Atomic Energy Agency, Vienna, 1988.

(Va75) A. Van Ginneken and M. Awschalom, *High energy particle interactions in large targets: Volume I, hadronic cascades, shielding, and energy deposition*, Fermilab (1975).

(Va87) A. Van Ginneken, P. Yurista, and C. Yamaguchi, "Shielding calculations for multi-TeV hadron colliders, Fermilab Report FN-447 (1987).

(Yu83) P. M. Yurista and J. D. Cossairt, "Concrete shielding exterior to iron," Fermilab Report TM-1204, Fermi National Accelerator Laboratory (1983).

(Za87) J. M. Zazula, "Derivation of accelerator shielding parameters from adjoining high energy neutron transport calculations", in *Theory and practices in radiation protection and shielding*, Proceedings of the Radiation Protection and Shielding Division, American Nuclear Society, Knoxville, Tennessee, April 22-24, 1987, Vol 2, pp.434-443.

Problems

1. It is asserted that if the assumption is made that the limiting attenuation is simply geometric, with the nucleon radius equal to 1.2 x 10^{-13} cm, then $\rho\lambda_{atten} = 38A^{1/3}$ (g/cm^2). Show this to be the case using the volume of a nucleus and nucleons along with the cross section.

2. a) Use the Moyer Model to calculate the dose equivalent rate (mrem/hr) lateral (θ = 90°) to a magnet centered in a 1.5 m radius tunnel. The magnet is struck by 10^{12} protons at 100 GeV (per sec). The tunnel walls consist of 1/3 m concrete followed by soil having the same composition [ρ(concrete) = 2.5 g/cm^3, ρ(soil) = 2.0 g/cm^3]. Perform the same calculation for several thicknesses of soil out to 6 meters of soil radially. Do this for increments of 1 meter from 1 meter to 6 meters of soil.

   b) Calculate the result if the same beam loss occurs uniformly over a string of such magnets 100 meters long in the same tunnel at the same soil thicknesses as above. Use the Tesch approximation. Approximately how many meters of beam loss does it take to cause 90% of the calculated dose equivalent rate at 6 m of lateral soil shield?

   c) For the point loss in part a), at what value of θ does the maximum dose equivalent rate occur and what is its magnitude outside of 6 meters of soil shield? (Use successive approximations to solve.)

3. An accelerator delivers 10^{12} 1 TeV protons per second head-on on the inner edge of a magnet as described in Fig. 3.15a. Use the CASIM calculations displayed in that figure to determine the approximate dose equivalent rate at R = 400 centimeters and compare with a result using the Moyer equation for point loss. Both calculations should be at the location of the maximum dose equivalent. Assume ρ(concrete) = 2.5 g/cm^3 and ρ(soil) = 2.25 g/cm^3. Why might there be an explainable disagreement between the two results?

4. Using the results of Monte-Carlo hadron calculations (FLUKA/MARS), calculate, for solid shields of iron (cylinders), what longitudinal thickness of iron is needed to achieve the same hadron dose equivalent per proton on the beam axis as found at R = 50 cm at 10 GeV/c, 100 GeV/c, 1000 GeV/c and 10 TeV/c. Use the maximum value of H (r = 50 cm).

5. In the Chapter 1, Fig. 1.20, we have calculations of neutron energy spectra for 200 MeV protons incident on various targets, including aluminum. In Fig. 3.10, calculations of dose equivalent values for concrete shielding surrounding aluminum targets at E_p = 200 MeV are given. At shielding thicknesses approaching zero and at forward angles, are the two results in "sensible" (that is, approximate, agreement)? (Hint: "Integrate" crudely over the forward spectrum to obtain the fluence/proton and convert this fluence to dose equivalent.)

   a) Make the comparison for zero shield thickness and in the angular range $0 < \theta < 30^o$.

   b) Now use the shielding calculations to obtain the dose equivalent rate (rem/h) due to a 1 μA beam incident at 200 MeV on such a thick target at a distance of 4 m from the target with 0, 1, 2, & 3 m of intervening concrete shielding (ρ = 2.5g/cm^3) for $\theta = 15^o$ and $\theta = 75^o$. (Hint: Use the center of the angular bins.)

6. Assume that a target is struck by 100 GeV protons and that a 10 m long decay space exists for π and K decay. Use the curves in Fig. 3.16 to crudely estimate the muon flux density and dose equivalent rates (mrem/h) at 1 km away and at $\theta = 0^o$ if 10^{12} protons/second are targeted in this manner if the following additional assumptions are made:

   a) Assume that there is no shielding present (neglect air scattering and in-scattering from the ground). (Hint: The muon yield for this decay space will scale with the length of the decay space.)

   b) Assume there is 100 meters of intervening shielding of earth (ρ = 2 g/cm^3) (Hint: use Fig. 1.14 range-energy curves to determine the mean energy of muons which will penetrate this much shielding). Neglect multiple scattering and range-straggling.

   c) If the beam operates for 4000 h/yr, is 100 mrem/yr exceeded? Will multiple scattering increase or decrease this dose equivalent? (Answer both questions for the soil-shielded case only.)

   d) Repeat Part b) of the same calculation using Sullivan's semi-empirical approach. If the disagreement between the results obtained using the two methods is large, suggest an explanation of a possible cause of the difference.